J. Fluid Mech. (2025), *vol.* 1017, A35, doi:10.1017/jfm.2025.10171

JFM PAPERS

A new dynamic slip approach for wall-modelled large eddy simulations in a consistent discontinuous Galerkin framework

Pratikkumar Raje[1] and **Karthik Duraisamy**[1]

[1]Department of Aerospace Engineering, University of Michigan, Ann Arbor, MI 48109, USA

Corresponding author: Pratikkumar Raje, praje@umich.edu

(Received 17 May 2024; revised 6 January 2025; accepted 23 April 2025)

A wall-modelled large eddy simulation approach is proposed in a discontinuous Galerkin (DG) setting, building on the slip-wall concept of Bae *et al.* (*J. Fluid Mech.*, vol. 859, 2019, pp. 400–432) and the universal scaling relationship by Pradhan and Duraisamy (*J. Fluid Mech.,* vol. 955, 2023, A6). The effect of the order of the DG approximation is introduced via the length scales in the formulation. The level of under-resolution is represented by a slip Reynolds number and the model attempts to incorporate the effects of the numerical discretization and the subgrid-scale model. The dynamic part of the new model is based on a modified form of the Germano identity – performed on the universal scaling parameter – and is coupled with the dynamic Smagorinsky model. A sharp modal cutoff filter is used as the test filter for the dynamic procedure, and the dynamic model can be easily integrated into any DG solver. Numerical experiments on channel flows show that grid independence of the statistics is achievable and predictions for the mean velocity and Reynolds stress profiles agree well with the direct numerical simulation, even with significant under-resolution. When applied to flows with separation and reattachment, the model also consistently predicts one-point statistics in the reverse flow and post-reattachment regions in good agreement with experiments. The performance of the model in accurately predicting equilibrium and separated flows using significantly under-resolved meshes can be attributed to several aspects that work synergistically: the optimal finite-element projection framework, the interplay of the scale separation and numerical discretization within the DG framework, and the consistent dynamic procedures for subgrid and wall modelling.

Key words: turbulence simulation, turbulent boundary layers, turbulent flows

1. Introduction

Wall-bounded turbulent flows are of particular relevance to many engineering applications. Computational costs of large eddy simulations (LES) increase significantly with the increase in Reynolds number. This is especially true for flows at a friction-velocity-based (u_τ) Reynolds number $Re_\tau > 10^3$, which is the range of Reynolds numbers relevant to industrial applications (Smits & Marusic 2013). A direct numerical simulation (DNS) resolves all the relevant scales of motion and offers the highest possible fidelity (Moin & Mahesh 1998). However, substantial grid requirements along with time-step limitations at high Reynolds numbers make DNS infeasible for computing flows of practical relevance. On the other hand, Reynolds-averaged Navier–Stokes (RANS) equations model all the relevant scales of motion and places less restrictive demands on computational costs but offers a lower fidelity (Wilcox 1998). It may not be a reliable tool for computing flows for which the turbulence models are not calibrated.

A wall-resolved LES (WRLES) resolves dynamically important energy-carrying eddies and models the nearly universal and nearly isotropic small-scale structures, i.e. subgrid scales (SGS) (Sagaut 2005). For a WRLES of a turbulent boundary layer at high Reynolds number, however, a vast majority of the computational resources have to be spent on the viscous and logarithmic layers since the grid point requirement for each of these layers scale as $O(Re_\tau^2)$ (Larsson *et al.* 2016). To alleviate this ‘near-wall problem of LES’, wall-modelled LES (WMLES) offers a practical solution, which aims to bypass the resolution of the inner layer of the turbulent boundary layers. In WMLES, turbulent motions in the inner layer are modelled, whereas outer layer turbulent motions are resolved as in a conventional LES (Piomelli & Balaras 2002). Wall-stress models and hybrid LES/RANS are the two different approaches to model the inner layer and perform WMLES. As these approaches still resolve the outer layer of the turbulent boundary layer, they can – in principle – offer better fidelity than RANS techniques.

A hybrid RANS/LES technique, including the detached eddy simulation in a WMLES set-up, uses RANS equations in the inner layer to estimate the wall stress and switches to the LES mode in the outer layer (Heinz 2020). The LES solution is used to feed information to a RANS model at some distance away from the wall. The predictions, however, depend on the choice of the RANS model and the modelling of the RANS/LES interface (Piomelli *et al.* 2003; Davidson & Dahlström 2005; Davidson & Billson 2006; Keating & Piomelli 2006; Shur *et al.* 2008; Choi, Edwards & Baurle 2009). On the other hand, a wall-stress model computes wall shear stress using a log law or the solution of some form of thin boundary layer equations (TBLE) on an embedded grid between the first grid point and the wall (Larsson *et al.* 2016; Bose & Park 2018). In this approach, the filtered wall shear stress is estimated at each time step using the LES information from an off-wall grid point on an LES mesh. The wall shear stress is then passed onto the LES grid as a Neumann boundary condition. Several wall-stress modelling strategies with varying complexities have been developed and studied over the years (Deardorff 1970; Schumann 1975; Piomelli *et al.* 1989; Piomelli 1999; Cabot & Moin 2000; Piomelli & Balaras 2002; Sagaut 2005; Piomelli 2008; Larsson *et al.* 2016; Bose & Park 2018).

A traditional algebraic equilibrium wall-stress model (EQWM) using a log law, e.g. Reichardt’s profile (Reichardt 1951), has the advantage of low computational cost. However, it generally performs poorly in non-equilibrium conditions and complex geometries, in particular, involving flows with boundary layer separation (Park 2017; Goc, Bose & Moin 2020; Whitmore, Bose & Moin 2024). Moreover, non-monotonic grid convergence in the prediction of the size of turbulent separation bubbles is also observed for the EQWMs (Goc *et al.* 2020; Whitmore *et al.* 2021; Agrawal *et al.* 2022). On the other hand, several non-equilibrium wall models have shown promise in predicting separated flows (Balaras, Benocci & Piomelli 1996; Wang & Moin 2002; Hickel *et al.* 2013; Park & Moin 2014, 2016*a*). However, the two-layer zonal wall models employing embedded grids require some effort in grid generation and domain decomposition in the pre-processing step, especially on unstructured meshes (Bodart & Larsson 2011; Park & Moin 2016*a*,*b*). The model predictions obtained using a wall-stress model depend on the choice of the exchange location (EL), i.e. the location from which the instantaneous LES solution is sampled to feed into the wall model, even for the simple geometry of a turbulent flow in a channel (Kawai & Larsson 2012; Frère *et al.* 2017). Consequently, the EL becomes a parameter of the simulation, which needs to be adjusted according to the flow field characteristics. Setting the EL requires knowledge of the boundary layer thickness, which is a property of the solution. Moreover, many of the wall-stress models introduce complexities with accompanying empiricism to treat complex flows, e.g. sensors to turn off the wall-stress models at the separation point (Bodart & Larsson 2011; Bose & Park 2018; Agrawal, Bose & Moin 2024).

Accurate and reliable prediction of separated flows at high Reynolds numbers remains a pacing research issue within the computational fluid dynamics (CFD) community. Several efforts to validate the state-of-the-art WMLES techniques in predicting separated flows at appropriate Reynolds numbers in a realistic external aerodynamics configuration have been undertaken recently. NASA CFD Vision 2030 report (Slotnick *et al.* 2014)) has identified WMLES for complex three-dimensional flows of practical relevance as one of the key milestones along the CFD technology development roadmap. Park & Moin (2016*b*), Lehmkuhl *et al.* (2018), Goc *et al.* (2020, 2021) have investigated predictive capabilities of equilibrium and non-equilibrium models within the WMLES framework in the characterization of the flow around an aircraft by considering the JAXA standard model and NASA common research model with wing/body/tail configuration, showing promise in practical applications, yet identifying several areas of improvement.

Since the solution may not be accurately computed near the wall on coarser near-wall LES grids due to the presence of steep wall-normal gradients, one promising alternative to the wall-stress models is the virtual-wall model in which the LES domain is terminated at some finite distance above the wall (Chung & Pullin 2009; Inoue & Pullin 2011; Cheng, Pullin & Samtaney 2015). Instantaneous slip velocities obtained using a reduced form of the TBLE are then provided at this virtual boundary or the ‘virtual wall’, which corresponds to the location of the bottom boundary in the LES. The offset of the virtual wall is set to be proportional to the mesh size. This treatment of the wall slip boundary condition has been shown to capture the quantitative features of a separation–reattachment turbulent boundary layer flow at low to moderately large Reynolds numbers. However, identification of the lifted virtual wall can be challenging for complex practical engineering geometric configurations.

Bose & Moin (2014) propose a wall modelling strategy in which formal boundary conditions for the filtered Navier–Stokes equations are derived instead of relying on the true (unfiltered) boundary conditions for the filtered fields. Unlike traditional wall-stress models and hybrid RANS/LES approaches, the method does not use a wall-stress model or a RANS model in the inner layer to estimate the wall stress. As a result, sampling of the LES solution at the off-wall grid points is not required. The model is derived using the properties of a modified form of the differential filter (Germano 1986), and it does not make any assumptions about the local state of the boundary layer or any RANS/LES hybridization. Instantaneous wall slip velocities can be estimated using this slip-wall model when the near-wall solution is under-resolved in the case of coarse grid resolutions. The model is compatible with an arbitrary LES filter and can be motivated using the RANS-type momentum equation (Yang & Bose 2017). It offers a promising alternative to the wall-stress models to predict high-Reynolds-number flows with complex geometries involving separation and reattachment.

The slip-wall model relates the velocity field at the wall to the wall-normal derivative of the velocity field via a wall-adjacent length scale called slip length. The slip length depends on a model coefficient C_w and the near-wall grid resolution $\varDelta$. The model recovers the no-slip condition as the near-wall grid is refined and in the limit $\varDelta \to 0$, and smoothly admits a wall slip velocity as the near-wall grid resolution is coarsened and the flow is no longer fully resolved. The slip-wall model is a general boundary condition applicable to any geometrically complex surface, including two orthogonally or non-orthogonally intersecting walls. Moreover, it is naturally suited to handle boundary layer separation as it will smoothly revert to a no-slip condition at the separation point without additional sensors or damping functions.

The value of the model parameter, i.e. the slip length, is found to depend on the Reynolds number Re_τ of the flow, grid resolution, SGS model and the numerical discretization (Carton & Murman 2017; Bae *et al.* 2019; Pradhan & Duraisamy 2023). Bose & Moin (2014) proposed a dynamic procedure to calculate the slip length based on the Germano identity. However, attempts to reproduce the results for a high Re_τ channel flow were unsuccessful (Bae *et al.* 2019). The wall-stress invariant dynamic wall model (WSIM) of Bae *et al.* (2019) provides an alternate dynamic procedure to estimate the slip length. The model predictions for the channel flow at the high Re_τ cases are found to depend on the grid resolution and grid convergence studies were not carried out. Numerical experiments with arbitrary constant values of slip length using NASA's discontinuous Galerkin (DG) solver eddy in the implicit LES set-up failed to yield stable computations when applied to a channel flow at $Re_\tau \gtrsim 1000$ with a high-order polynomial basis ($p = 3$ and $p = 7$) (Carton & Murman 2017).

Existing dynamic versions of the slip-wall model of Bose & Moin (2014), Bae *et al.* (2019) are found to be sensitive to the numerical implementation details, including the numerical discretization and the choice of SGS model in a finite-volume framework. Moreover, some models (Bae *et al.* 2019) show a significant log-layer mismatch with the DNS. Given the limitations of the existing dynamic slip-wall models, recent works use a Prandtl mixing length-based model to estimate slip lengths (Whitmore *et al.* 2024). Other strategies to estimate optimal slip lengths include an optimization procedure to reproduce a known wall shear stress distribution for turbulent channel flows at a range of Reynolds numbers and grid resolutions and model the behaviour of the slip lengths using a curve fit (Whitmore & Bose 2023). *Ad hoc* sensor-based modelling strategies to change the model forms for the slip lengths that switch between the mixing-length-based and parameterized forms in the separation regions have also been studied (Whitmore *et al.* 2024). Application of the static slip-length models to separated flows in the Boeing speed bump and the JAXA standard model configurations suggests that robust separation predictions require the development of an accurate method for computing slip lengths.

Pradhan & Duraisamy (2023) employed an optimal finite-element projection framework to obtain *a priori* estimates of the wall slip velocity for a typical WMLES using DNS data for a channel flow (Lee & Moser 2015) and proposed improvements to the slip-wall model of Bose & Moin (2014). The optimal projection framework is used to modify the slip length, and it is represented as a function of the Reynolds number based on local slip-velocity magnitude and near-wall local grid resolution Re_{slip}. A new model parameter λ is introduced to represent the effect of the numerical method or the order of projection p in the DG set-up and SGS model. Using an *a priori* estimate for λ, the Re_{slip} model for the modified slip length is shown to give good predictions for a range of high Re_τ channel flow cases with the constant coefficient Smagorinsky SGS model using a DG solver with orders of projection up to $p = 3$.

The present study begins with the modified form of the slip-wall model proposed by Pradhan & Duraisamy (2023), which uses the Re_{slip} model for the modified model coefficient. The main objective is to establish a dynamic modelling procedure for the model parameters. We use the dynamic Smagorinsky model (DSM) as the SGS model (Germano *et al.* 1991). The choice of the SGS model is found to be critical to obtain the correct slope of the velocity profile in the log layer (Bae *et al.* 2019). On the other hand, values of the slip length are found to be responsible for a shift in the mean velocity profile relative to the DNS data, and they do not affect the shape of the mean velocity profile.

The paper is organized as follows. Section 2 presents the DG discretization framework used in the present work. Section 3 provides an overview of the original slip-wall model formulation by Bose & Moin (2014) along with the modification introduced by Pradhan & Duraisamy (2023). The dynamic modelling procedures of Bose & Moin (2014) and Bae *et al.* (2019) to calculate the slip length are discussed briefly in § 4. The proposed dynamic modelling strategy to estimate the model parameter λ using a modified form of the Germano identity and the Re_{slip} model is presented in § 5. The key assumptions to arrive at the final form of the dynamic model are also discussed. The proposed dynamic slip-wall model is tested on a range of channel and periodic hill flows in § 6 and results are compared with the available DNS and experimental data along with an EQWM. Finally, conclusions are drawn in § 7.

2. Discontinuous Galerkin discretization

The governing equations in this work are the compressible Navier–Stokes equations in their conservative form written as

$$\frac{\partial \mathbf{U}}{\partial t} + \nabla \cdot \mathbf{F}(\mathbf{U}) - \nabla \cdot \mathbf{G}(\mathbf{U}, \nabla \mathbf{U}) = \mathbf{0}, \tag{2.1}$$

where $\mathbf{U} \in \mathbb{R}^s$ is the conservative state vector of rank s, consisting of density, momentum and total energy components, $\mathbf{F}$ is the inviscid flux and $\mathbf{G}$ is the viscous flux. We note that boldface denotes a state vector. We use the DG method for the spatial discretization. The DG method combines the concepts of finite-element and finite-volume methods and allows for high-order approximations, geometric flexibility and natural parallelization. The computational domain $\varOmega$ is divided into non-overlapping elements K, each having a subdomain $\varOmega_K$ and boundary $\partial \varOmega_K$. These elements can have arbitrary shapes and sizes, allowing for efficient representation of complex geometries. A polynomial approximation is typically used to represent the solution using a L_2 projection within each element. The degree of the polynomial p can vary, and higher-degree polynomials enable higher-order accuracy. The DG space $\mathcal{V}_h$ is defined as

$$\mathcal{V}_h \triangleq \left\{ \phi \in L_2(\varOmega) : \phi_h \equiv \phi|_{\varOmega_K} \in P^p, \forall \varOmega_K \in \varOmega \right\}, \tag{2.2}$$

where the space of polynomials up to degree p is denoted as P^p and ϕ_h is the basis function defined on $\varOmega_K$. Defining $\mathcal{V}_h$ in this manner allows for discontinuities in the solution across element boundaries. The elementwise solution $\mathbf{U}_h$ that approximates $\mathbf{U}$ in $\varOmega_k$ takes the form

$$\mathbf{U}(\mathbf{x}, t) \approx \mathbf{U}_h(\mathbf{x}, t) = \sum_{j=1}^{n_p} \mathbf{W}_{k,j}(t) \phi_{k,j}(\mathbf{x}), \quad \mathbf{x} \in \varOmega_k, \tag{2.3}$$

where $\mathbf{U}_{k,j}$ represents the coefficients associated with the jth basis function $\phi_{k,j}$ and n_p represents the total number of degrees of freedom within the element k of order p.

The DG method employs a weak formulation of the governing equations that is obtained by multiplying (2.1) by test functions, which are the same as the basis functions, integrating by parts and coupling the elements via numerical fluxes:

$$\begin{aligned}
&\int_{\Omega_K} \phi_h^T \frac{\partial \mathbf{U}_h}{\partial t}\,\mathrm{d}\Omega - \int_{\Omega_K} \nabla\phi_h^T \cdot [\mathbf{F}(\mathbf{U}_h) - \mathbf{G}(\mathbf{U}_h, \nabla\mathbf{U}_h)]\,\mathrm{d}\Omega \\
&\quad + \int_{\partial\Omega_K} \phi_h^T \left[\widehat{\mathbf{F}}\left(\mathbf{U}_h^+, \mathbf{U}_h^-\right) - \widehat{\mathbf{G}}\left(\mathbf{U}_h^+, \mathbf{U}_h^-, \nabla\mathbf{U}_h^+, \nabla\mathbf{U}_h^-\right)\right]\cdot\mathbf{n}\,\mathrm{d}S \\
&\quad - \int_{\partial\Omega_K} \left(\mathbf{U}_h^+ - \{\mathbf{U}_h\}\right)^T \mathbf{G}\left(\mathbf{U}_h^+, \nabla\phi_h^+\right)\cdot\mathbf{n}\,\mathrm{d}S = \mathbf{0} \quad \text{for all } \phi_h \in \boldsymbol{\mathcal{V}}_h.
\end{aligned} \tag{2.4}$$

Here $\partial\Omega_K$ represents the element boundary and, on that boundary, $(\cdot)^+$ and $(\cdot)^-$ represent quantities taken from the current and neighbouring element, respectively. Approximate numerical fluxes are denoted by $\widehat{(\cdot)}$, $\{\cdot\}$ represents a face average or boundary value and $\mathbf{n}$ is the outward pointing normal vector. The boundary conditions are set through the numerical fluxes.

Substituting (2.3) into (2.4), we get the final update equation that can be written as

$$\mathbf{M}\frac{\mathrm{d}\mathbf{W}}{\mathrm{d}t} = -\mathbf{RHS}, \tag{2.5}$$

where $\mathbf{M}$ is the spatial mass matrix and $\mathbf{RHS}$ consists of the volume and surface integrals. Then, the spatial residual vector can be defined as

$$\mathbf{R} \equiv \frac{\mathrm{d}\mathbf{W}}{\mathrm{d}t} = -\mathbf{M}^{-1}\mathbf{RHS}. \tag{2.6}$$

We solve for the expansion coefficients $\mathbf{W}$ that then provide an approximation of the solution to the governing equations over the entire computational domain. The solver used in the present study is discussed in § 6 and Appendix A.

3. Slip-wall modelling

The slip-wall model is essentially a wall boundary condition. The main idea is that the slip velocity is a natural consequence of the near-wall under-resolution of the LES mesh. This has also been shown by Pradhan & Duraisamy (2023) using the optimal finite-element projection framework wherein the L_2 projection of channel flow DNS data onto grids suitable for a WMLES results in slip velocities at the wall. Also, the magnitude of the slip velocity is shown to increase with an increase in near-wall grid under-resolution. This shows that the near equivalence in the boundary conditions for the unfiltered and filtered variables does not hold in the case of a coarse LES when wall modelling becomes necessary. A slip-wall model is an alternative to the traditional wall-stress modelling approach wherein the wall stress is not estimated directly but is indirectly affected through the non-vanishing filtered velocities at the wall. It provides estimates of the slip velocities at the wall when the LES grid resolution is insufficient to accurately resolve the near-wall region and the no-slip condition is not satisfied.

Bose & Moin (2014) use the properties of a modified differential filter to derive a slip-velocity boundary condition given as

$$\overline{u}_i = \overline{C}_w \overline{\Delta}_w \frac{\partial \overline{u}_i}{\partial n}, \tag{3.1}$$

where n is the wall-normal direction, $\overline{C}_w$ is a tunable model coefficient, whereas $\overline{\varDelta}_w$ is related to the near-wall grid resolution. In (3.1) the slip velocity only depends on the wall-normal derivative of the velocity field and is a direct consequence of the constraint placed on the differential filter that the slip length vanishes at the boundaries. The magnitude of the slip length, i.e. $\overline{C}_w\overline{\varDelta}_w$, imposes a filter length scale at the wall; if it vanishes at the wall then the filtered velocity field will exactly satisfy a no-slip boundary condition. The slip-wall boundary condition smoothly admits a wall slip velocity as the near-wall LES resolution is coarsened and the flow is no longer fully resolved. It is pertinent to note that while (3.1) is derived from a specific choice of the form of the filter kernel, previous studies (Carton & Murman 2017; Pradhan & Duraisamy 2023) show that the slip-wall model can still perform well even without using the specified filter explicitly.

Pradhan & Duraisamy (2023) characterize the wall slip velocity in a WMLES in terms of a Reynolds number based on slip-velocity magnitude and near-wall under-resolution using the optimal finite-element projection framework and propose a modified form of the slip-wall model given by

$$\overline{u}_i = \frac{\overline{C}_{w,\lambda}}{\lambda}\overline{\varDelta}_w\frac{\partial \overline{u}_i}{\partial n}, \quad \text{where } \overline{C}_w = \frac{\overline{C}_{w,\lambda}}{\lambda}. \tag{3.2}$$

The model coefficient $\overline{C}_{w,\lambda}$ is a function of the slip-velocity-based Reynolds number $\overline{Re}_{slip}$ and λ, where $\overline{Re}_{slip} = \overline{u}_s(\overline{\varDelta}^e_w/p)/\overline{\nu}$. Here, $\overline{u}_s$ is the magnitude of the wall slip velocity and $\overline{\nu}$ is the kinematic viscosity of the fluid. Note that p denotes the order of the polynomial basis used in the DG solver with $\overline{\varDelta}^e_w$ being the element size adjacent to the wall, and their ratio represents the effective grid size. The model parameter λ contains the effect of the order of projection p and, hence, the numerical method along with the SGS model. Using the above form of $\overline{C}_{w,\lambda}$, it is found that given an SGS model $\overline{C}_{w,\lambda}/\lambda$ admits a universal scaling relationship for a particular value of λ for a wide range of the parameter space. As a result, the model incorporates the effect of Reynolds number, near-wall grid under-resolution, SGS model and numerical discretization.

4. Previous dynamic slip-wall models

Bose & Moin (2014) presented a dynamic procedure to compute the slip length ($\overline{C}_w\overline{\varDelta}_w$) in the slip-wall model given by (3.1). It uses a modified form of the Germano identity, which represents the invariance of the total Reynolds stress at the test-filtered level. The model coefficient ($\overline{C}_w\overline{\varDelta}_w$) is computed as

$$\left(\overline{C}_w\overline{\varDelta}_w\right)^2 \varDelta_R^2 \frac{\partial \widehat{\overline{u}}_i}{\partial n}\frac{\partial \widehat{\overline{u}}_j}{\partial n} + T_{ij} - \widehat{\tau}_{ij} = \widehat{\overline{u}_i\overline{u}_j} - \widehat{\overline{u}}_i\widehat{\overline{u}}_j, \tag{4.1}$$

where $\varDelta_R = (\widehat{\overline{\varDelta}}_w/\overline{\varDelta}_w)$ is the ratio of the test filter width to the grid filter width at the wall, and a value of $\varDelta_R = 1.4$ is recommended. Here, $\overline{(\cdot)}$ represents a grid-filtered quantity, a hat, i.e. $\widehat{(\cdot)}$, denotes the test filtering operation, T_{ij} and τ_{ij} depict the SGS stress tensors at the test and grid filter levels, respectively. The slip length is assumed to be equal for the three spatial directions. Equation (4.1) is solved for ($\overline{C}_w\overline{\varDelta}_w$) using a least squares method. The model was tested on a series of high-Reynolds-number channel flows and NACA 4412 airfoil at near-stall conditions.

Bae *et al.* (2019) proposed an alternate dynamic modelling strategy for the slip length ($\overline{C}_w\overline{\varDelta}_w$) as an improvement over the Bose & Moin (2014) dynamic model. The dynamic model is based on a combination of the invariance of the wall-stress condition under test filtering and a modified form of the Germano identity and is referred to as the wall-stress invariant model (WSIM). The proposed dynamic modelling approach, however, is not unique, and different modelling choices are possible. The dynamic model is given by

$$\left(\overline{C}_w\overline{\varDelta}_w\right)^2=\frac{L_{ij}M_{ij}+F_{ij}M_{ij}}{M_{kl}M_{kl}}, \tag{4.2}$$

where

$$L_{ij}=\overline{u}_i\overline{u}_j-\widehat{\overline{u}}_i\widehat{\overline{u}}_j, \tag{4.3}$$

$$M_{ij}=\left[\frac{\partial\overline{u}_i}{\partial n}\frac{\partial\overline{u}_j}{\partial n}-\varDelta_R^2\frac{\partial\widehat{\overline{u}}_i}{\partial n}\frac{\partial\widehat{\overline{u}}_j}{\partial n}\right], \tag{4.4}$$

and F_{ij} contains different wall stresses, namely Reynolds stress, subgrid stress, viscous stress and pressure tensors computed from the specified velocity field. The model was tested on a statistically stationary plane turbulent channel, a non-equilibrium three-dimensional transient channel and a zero-pressure-gradient flat-plate turbulent boundary layer.

5. A new dynamic slip-wall model

We propose a dynamic procedure to compute the model coefficient λ in the modified slip-wall model given by (3.2) rather than the slip length in (3.1) following insights from Pradhan & Duraisamy (2023). We start with the Germano identity (Germano *et al.* 1991), which can be written as

$$T_{ij}-\widehat{\tau}_{ij}=\widehat{\overline{u}_i\overline{u}_j}-\widehat{\overline{u}}_i\widehat{\overline{u}}_j, \tag{5.1}$$

where the SGS stresses at the grid and test-filtered levels are given by

$$\tau_{ij}=\overline{u_iu_j}-\overline{u}_i\overline{u}_j \quad \text{and} \quad T_{ij}=\widehat{\overline{u_iu_j}}-\widehat{\overline{u}}_i\widehat{\overline{u}}_j. \tag{5.2}$$

Equation (5.1) represents an exact identity and does not involve any assumptions. Subtracting $(\widehat{\overline{u}_i\overline{u}_j}-\overline{u}_i\overline{u}_j)$ from both sides of (5.1), we get

$$T_{ij}-\widehat{\tau}_{ij}-(\widehat{\overline{u}_i\overline{u}_j}-\overline{u}_i\overline{u}_j)=\overline{u}_i\overline{u}_j-\widehat{\overline{u}}_i\widehat{\overline{u}}_j. \tag{5.3}$$

We assume that the slip velocity at the test-filtered level takes a form similar to that for the grid-filtered level, and it is given by

$$\widehat{\overline{u}}_i=\widehat{\overline{C}}_w\widehat{\overline{\varDelta}}_w\frac{\partial\widehat{\overline{u}}_i}{\partial n}, \tag{5.4}$$

where the model coefficient $\widehat{\overline{C}}_w=\widehat{\overline{C}}_{w,\lambda}/\lambda$ has a form similar to that of the coefficient at the grid-filtered level $\overline{C}_w=\overline{C}_{w,\lambda}/\lambda$. Next, we assume that λ is constant between the grid and test-filtered levels. This assumption is based on the findings of Pradhan & Duraisamy (2023) using the optimal finite-element projection framework. The universality of the model coefficient λ depends on the choice of the length scale $\varDelta_w$ used in the slip-wall model. If the cube root of the cell volume is used as the length scale, λ is found to remain fairly constant across different resolutions and Reynolds numbers for a given SGS model. Next, we assume the slip length to be equal in the streamwise and spanwise directions, while zero in the wall-normal direction, i.e. no transpiration based on the findings of Pradhan & Duraisamy (2023). In general, it can be different in the streamwise, spanwise and wall-normal directions as observed in the *a priori* studies on the slip-wall model using the optimal finite-element projection framework by Pradhan & Duraisamy (2023). However, numerical experimentation using arbitrary constant values of the slip lengths in the streamwise and spanwise directions for turbulent channel flows did not significantly affect the model predictions. Similar observations are made in the numerical experiments of Bae *et al.* (2019). Notably, in the previous works on dynamic slip-wall models (Bose & Moin 2014; Bae *et al.* 2019), slip length is assumed to be the same in the three spatial directions.

The model coefficient $\widehat{\overline{C}}_{w,\lambda}$ is assumed to be a function of Reynolds number based on slip-velocity magnitude and the near-wall grid resolution at the test-filtered level along with λ. Substituting for the slip velocities at the grid-filtered level and test-filtered level using (3.1) and (5.4) on the right-hand-side of (5.3), we get

$$\left(\overline{C}_w\overline{\Delta}_w\right)^2 \frac{\partial \overline{u}_i}{\partial n}\frac{\partial \overline{u}_j}{\partial n} - \left(\widehat{\overline{C}}_w\widehat{\overline{\Delta}}_w\right)^2 \frac{\partial \widehat{\overline{u}}_i}{\partial n}\frac{\partial \widehat{\overline{u}}_j}{\partial n} = \overline{u}_i\overline{u}_j - \widehat{\overline{u}}_i\widehat{\overline{u}}_j\,. \tag{5.5}$$

Now, $\overline{\Delta}_w$ and $\widehat{\overline{\Delta}}_w$ depend on the grid resolution, p, and the filter used. On the other hand, the model coefficients $\overline{C}_w$ and $\widehat{\overline{C}}_w$ depend on Re_{slip}, p at the grid- and test-filtered levels, respectively, and the model coefficient λ. In principle, we can use the above equation to find λ for a given model for $\overline{C}_w$ and, hence, $\widehat{\overline{C}}_w$. However, this would result in a significantly complex nonlinear equation in λ. We choose an alternate approach to simplify the process with an aim to keep a balanced mixture of physical content and mathematical simplicity and rewrite (5.5) as

$$\left(\overline{C}_w\overline{\Delta}_w\right)^2 \left[\frac{\partial \overline{u}_i}{\partial n}\frac{\partial \overline{u}_j}{\partial n} - C_{wR}^2\Delta_R^2 \frac{\partial \widehat{\overline{u}}_i}{\partial n}\frac{\partial \widehat{\overline{u}}_j}{\partial n}\right] = \overline{u}_i\overline{u}_j - \widehat{\overline{u}}_i\widehat{\overline{u}}_j, \tag{5.6}$$

where $C_{wR} = \widehat{\overline{C}}_w/\overline{C}_w$. In this work, we use the value for Δ_w as per Pradhan & Duraisamy (2023) and Δ_R is given by

$$\Delta_R = \frac{\widehat{\overline{\Delta}}_w}{\overline{\Delta}_w} = \frac{p}{p^\star}, \tag{5.7}$$

where $p^\star$ is the sharp modal cutoff filter order, as discussed in Appendix A. On the other hand, Pradhan & Duraisamy (2023) show that the model coefficient $C_{w,\lambda}$ is a function of grid resolution, and its value increases when the grid resolution is changed from Δ^+ to $2\Delta^+$. In other words, given that the test filter width is coarser than the grid filter width, $\widehat{\overline{C}}_w$ can be expected to be greater than $\overline{C}_w$, thereby resulting in the ratio C_{wR} to be greater than one. We use a value of $C_{wR} = 2$ in this work. Sensitivity studies using different plausible values of C_{wR} are shown in Appendix C.

Let

$$M_{ij} = \left[\frac{\partial \overline{u}_i}{\partial n}\frac{\partial \overline{u}_j}{\partial n} - C_{wR}^2\Delta_R^2 \frac{\partial \widehat{\overline{u}}_i}{\partial n}\frac{\partial \widehat{\overline{u}}_j}{\partial n}\right] \quad \text{and} \quad L_{ij} = \overline{u}_i\overline{u}_j - \widehat{\overline{u}}_i\widehat{\overline{u}}_j \tag{5.8}$$

for notational convenience. Equation (5.6) can then be equivalently written as

$$\left(\frac{\overline{C}_{w,\lambda}}{\lambda}\overline{\Delta}_w\right)^2 M_{ij} = L_{ij}\,. \tag{5.9}$$

Equation (5.9) represents six independent equations in space for a single unknown λ given the model for $\overline{C}_{w,\lambda}$. Thus, the system is overdetermined and we use the method of least squares to obtain λ, which is then given by

$$\left(\frac{\overline{C}_{w,\lambda}}{\lambda}\overline{\varDelta}_w\right)^2 = max\left(\frac{\langle L_{ij}M_{ij}\rangle}{\langle M_{kl}M_{kl}\rangle}, 0\right), \tag{5.10}$$

where $\langle\rangle$ indicates that the numerator and denominator are first averaged over an element followed by an averaging over the directions of homogeneity, i.e. streamwise and spanwise in the case of channel flows and spanwise in the case of periodic flows, and the ratio is clipped to have a maximum value of zero. We can rewrite the above equation as

$$\frac{\overline{C}_{w,\lambda}}{\lambda}\overline{\varDelta}_w - l_s = 0, \tag{5.11}$$

where

$$l_s = \sqrt{max\left(\frac{\langle L_{ij}M_{ij}\rangle}{\langle M_{kl}M_{kl}\rangle}, 0\right)}. \tag{5.12}$$

Pradhan & Duraisamy (2023) provide a model fit for $\overline{C}_{w,\lambda}$ based on L_2 projected channel flow DNS data, which is given by

$$\overline{C}_{w,\lambda} = \begin{cases} 0.725\ log_{10}\ (\overline{Re}_{slip}/\lambda) - 0.925 & \text{if } \log_{10}(\overline{Re}_{slip}/\lambda) > 4.25, \\ 0.6\ log_{10}\ (\overline{Re}_{slip}/\lambda) - 0.41 & \text{if } \log_{10}(\overline{Re}_{slip}/\lambda) > 3.18, \\ 0.475\ log_{10}\ (\overline{Re}_{slip}/\lambda) - 0.003 & \text{if } \log_{10}(\overline{Re}_{slip}/\lambda) > 0.7, \\ 0.33 & \text{otherwise.} \end{cases} \tag{5.13}$$

Substituting for $\overline{C}_{w,\lambda}$ in (5.11), we get a nonlinear equation with λ as the only unknown, which can be found dynamically using a numerical method. The Secant method is used to find λ using (5.11) and (5.13). The parameter λ, thus obtained, can reach unrealistically high values, especially at high Reynolds numbers on coarse near-wall LES meshes. We prescribe an upper limit to λ as

$$\lambda_f = max(\lambda, 3\lambda_{CCSM}), \quad \text{where } \lambda_{CCSM} = 1.125. \tag{5.14}$$

Here, λ_{CCSM} is the value of λ for the constant coefficient Smagorinsky model obtained in the *a priori* analysis of channel flow DNS data and traditional wall model predictions using the optimal finite-element projection framework in Pradhan & Duraisamy (2023). The limiter value is based on numerical experimentation across the range of Reynolds numbers and flow configurations considered in this work. Finally, we use λ_f in (3.2).

The dynamic model in (5.11) is essentially identical to the dynamic slip-wall model of Bose & Moin (2014). The model given by (5.11) can be transformed to (4.1) using the Germano identity. However, the model form in (4.1) is found to be sensitive to the implementation details including the numerical discretization and the choice of the SGS model in a finite-volume framework in previous studies (Park & Moin 2016*b*; Bae *et al.* 2019). Our attempts to use this model form in the DG framework with $p \geqslant 2$ resulted in unstable simulations with the constant coefficient and the dynamic Smagorinsky SGS models.

We remark that the dynamic modelling procedure to obtain λ as discussed above is not unique. The model coefficient can be obtained using a number of modelling choices, e.g. modified form of the Germano identity used in Bae *et al.* (2019). Equation (5.10) has a form similar to that of the dynamic model of Bae *et al.* (2019), but it does not contain the additional wall-stress terms in the numerator, which originates from the invariance of the wall-stress condition under test filtering. Those additional wall-stress terms are expected to predict the same wall stress regardless of the grid resolution (or filter) and act as an effective self-regulating mechanism to control the changes in slip length to predict the correct wall stress. In our case, a similar effect is obtained by enforcing the Pradhan & Duraisamy (2023) model for $\overline{C}_{w,\lambda}$, which is a function of the slip-wall velocity and near-wall grid resolution via the slip-based Reynolds number. The parameter $\overline{C}_{w,\lambda}$ and, hence, the slip length appropriately changes when the near-wall grid is refined or coarsened and/or when the Reynolds number is increased or decreased, resulting in an appropriate change in the wall stress. Note that the wall stress can be related to the slip length $(\overline{C}_w \overline{\Delta}_w)$ and slip velocity U_{slip} using the slip-wall model as $\tau_w = (\nu + \nu_{SGS})(U_{slip}/(\overline{C}_w \overline{\Delta}_w))$, where ν_{SGS} is the SGS or eddy viscosity.

5.1. *Implementation of the wall boundary condition*

We assume that there is no transpiration and slip is only allowed in the wall-parallel directions. It is useful to note that, the slip-wall model allows for transpiration as considered in the previous studies of Bose & Moin (2014), Carton & Murman (2017) and Bae *et al.* (2019). However, using the optimal finite-element projection framework, Pradhan & Duraisamy (2023) show that the slip length associated with the wall-normal velocity is approximately zero. Hence, it can be set to zero without significant loss of generalizability. In the current implementation of the dynamic slip-wall model, we compute the wall-normal derivatives of the slip-velocity components at the wall using (3.2). The wall-parallel slip-velocity components at the wall are computed using the solution inside the element adjacent to the wall. This is then used to compute the wall stress and it is applied as a Neumann boundary condition complemented by a slip boundary condition for the velocity. The numerical implementation is done using the following steps.

(i) At every integration point, a ghost value is created, where the wall-parallel slip-velocity components at the wall are obtained from the element interior state $\mathbf{U}_h^+$ as

$$\overline{u}_{h,i}^b = \overline{u}_{h,i}^+ - \overline{u}_{h,j}^+ n_j n_i. \tag{5.15}$$

Wall-normal velocity gradients are also calculated using the interior solutions.

(ii) Slip-wall parameters $C_{w,\lambda}$ and λ are computed using the dynamic slip-wall model.

(iii) The wall-normal derivatives of the slip-velocity components at the wall are then computed using the slip-wall model given by (3.2) as

$$\left.\frac{\partial \overline{u}_{h,i}}{\partial n}\right|_w = \frac{\overline{u}_{h,i}^b}{\Delta (C_{w,\lambda}/\lambda)}. \tag{5.16}$$

(iv) Finally, wall-stress components at the quadrature points of the boundary faces are computed using

$$\tau_w' = (\nu + \nu_{SGS}) \left.\frac{\partial \overline{u}_{h,i}}{\partial n}\right|_w, \tag{5.17}$$

where we consider the contribution of the mean wall stress from the viscous and subgrid stresses for the wall stress.

(v) The projected wall stress $\tau_{w,i} = \tau_w' n_i$ is applied as a Neumann boundary condition.

6. Numerical experiments

In this work we use CaslabDG, an in-house DG solver for the computations. The governing equations are the filtered compressible Navier–Stokes equations in conservative form. The solver was successfully used previously to compute statistically stationary channel flows at high Re_τ (Pradhan & Duraisamy 2023) using a constant coefficient Smagorinsky model with up to 3 orders of the polynomial basis p. The solver is parallelized using the message passing interface (MPI). Inviscid fluxes are approximated using the Roe approximate Riemann solver (Roe 1981). An SGS model is used for the unresolved SGS stresses in the filtered Navier–Stokes equations. The SGS viscosity is added to the molecular viscosity and the viscous flux contains both molecular and turbulence contributions. The second form of Bassi and Rebay (Bassi & Rebay 2000), popularly known as the BR-2 scheme, is used for the viscous fluxes. The governing equations are marched in time using an explicit third-order Runge–Kutta total variation diminishing (RK3-TVD) scheme.

The solver uses the Lagrange nodal basis evaluated at the Gauss–Legendre quadrature points and the number of quadrature points ngp in each of the three directions is related to the polynomial degree of approximation by $ngp = (p+2)$. The integrals are approximated using the Gauss quadrature rule. The basis and test functions are created using a tensor product of the one-dimensional Lagrange interpolating polynomials that forms a non-hierarchical nodal basis. The corresponding number of degrees of freedom in each element is $(p+1)^3$. We use a Lagrange polynomial basis of degree $p=2$ for all the WMLES computations. It is to be noted that we do not use an explicit filter for the spatial filtering operation, but rely on implicit filtering through the numerical discretization and grid resolution. Also, the polynomial basis degree of $p=2$ used in this work does not warrant for polynomial dealiasing, which can be achieved by explicitly filtering the solution at every time step (Diosady & Murman 2013; Gassner & Beck 2013; Brazell *et al.* 2015).

The results obtained using the dynamic slip-wall model are compared with those obtained using an EQWM. For the EQWM, we compute the wall friction τ_w from the instantaneous velocity taken at the furthest distance from the wall inside the first element. The computed wall friction is then used as the Neumann boundary condition applied at the quadrature points of the boundary faces. Our implementation is similar to the work of Carton & Murman (2017). We use the Reichardt function of the form

$$u^+ = \frac{1}{\kappa} ln(1+\kappa z^+) + 6.646\left[1 - exp\left(\frac{-z^+}{11}\right) - \frac{z^+}{11} exp\left(\frac{-z^+}{3}\right)\right], \tag{6.1}$$

where $\kappa = 0.38$, as the EQWM, and use the Newton–Raphson method to iterate on the values of u^+ and y^+. This wall function supports the theoretical velocity profile down to the wall. We have chosen this approach for its simplicity and efficiency, and it is shown to give excellent results for statistically steady channel flows at high Reynolds numbers in Carton & Murman (2017). Note that, for the simulations of separated flows in periodic hill configuration, we do not use any adjustments to the implementation of the EQWM like turning off the model in the separation region.

6.1. *Sharp modal cutoff filter as a test filter*

The dynamic modelling procedure requires filtering at two different levels, i.e. grid filter and test filter, to calculate the value of the model coefficient λ. In a DG framework this is equivalent to using two different orders of polynomial basis for approximating the solution. The Lagrange interpolation polynomials, which are used as the basis functions within our work, are not hierarchical, i.e. every basis function contains high-order solution content. As a result, unlike a spectral method, we cannot directly use a sharp cutoff filter to remove the higher-order modes. To reduce the order of projection that would result in a coarser filtering operation, the solution coefficients need to be transformed to a modal representation, the hierarchical form of which allows for a classification of solution modes based on polynomial degree. The solution can then be coarsely filtered by setting the higher-order modes to zero or by scaling the higher-order coefficients by a factor $\alpha \in [0, 1]$. In this work, we use a cutoff filter order $p^\star = 1$ and set the modes of degree greater than one to zero for the test filter. This is equivalent to assuming a test filter to be about twice the width of the grid filter, which is generally followed in finite difference or finite-volume methods (Pope 2000). Once the filtered forms of modal solution coefficients are obtained, an inverse transformation is performed to get the filtered nodal solution coefficients, thereby obtaining the coarse-filtered solution. In this work, we follow the procedure outlined by Brazell *et al.* (2015) to implement the sharp modal cutoff filter in our solver, and it is discussed in detail in Appendix A.

6.2. *Dynamic Smagorinsky model*

The DSM is a simple eddy viscosity model that relates the unresolved SGS stresses to the resolved strain rate $\overline{S}_{ij}$ via a turbulent viscosity ν_{SGS} as

$$\tau_{ij}^{SGS} = 2\overline{\rho}\nu_{SGS}\overline{S}_{ij}, \quad \text{where } \overline{S}_{ij} = \frac{1}{2}\left(\frac{\partial \overline{u}_i}{\partial x_j} + \frac{\partial \overline{u}_j}{\partial x_i}\right). \tag{6.2}$$

The SGS eddy viscosity is related to a characteristic velocity and a length scale on dimensional grounds, and it is given by

$$\nu_{SGS} = (C_S \varDelta)^2 |\overline{S}|, \tag{6.3}$$

where C_S is the Smagorinsky coefficient, $|\overline{S}| = \sqrt{2\overline{S}_{ij}\overline{S}_{ij}}$ is the strain-rate magnitude and $\varDelta$ is the filter width or a representative grid size. The DSM improves upon the original Smagorinsky model by dynamically adjusting the model coefficient ($C_S \varDelta$) based on local flow properties. The idea is to seek a more accurate representation of the turbulence, especially in regions with varying flow conditions. The DSM also provides a near-wall correction that can lead to proper near-wall behaviour of the SGS viscosity without the use of wall-damping functions. The dynamic calculation of the coefficient is based on an explicitly performed second-level filter operation called the test filter that is applied to the grid-filtered variables. As mentioned before, we denote the test filter operation by a hat and we use the sharp modal cutoff filter as the test filter, as discussed in (6.1). The model coefficient ($C_S \varDelta$) is calculated as

$$(C_s \varDelta)^2 = \frac{1}{2}\frac{L_{ij}^d M_{ij}}{M_{kl} M_{kl}}, \tag{6.4}$$

where the Leonard stress tensor L_{ij} and its deviatoric part L_{ij}^d are given by

$$L_{ij} = \widehat{\overline{u}_i \overline{u}_j} - \widehat{\overline{u}}_i \widehat{\overline{u}}_j, \quad L_{ij}^d = L_{ij} - \frac{1}{3} L_{kk}\delta_{ij} \tag{6.5}$$

and

$$M_{ij} = \widehat{|\overline{S}|\overline{S}_{ij}} - \varDelta_R^2 |\widehat{\overline{S}}| \widehat{\overline{S}}_{ij}\,. \tag{6.6}$$

The derivative and the test filter operations do not commute for the sharp modal cutoff filter. We follow Brazell *et al.* (2015) to determine the second term of M_{ij} by computing the test-filtered velocity followed by the derivatives of the test-filtered velocity to form the strain-rate tensor. Another possible choice is to use the test filter operation on the grid-filtered strain rate, but this approach does not have any advantages over the method used here as shown by Brazell *et al.* (2015). The parameter Δ_R is calculated as per the recommendation of Brazell *et al.* (2015) and it is given by

$$\Delta_R = \frac{\widehat{\overline{\Delta}}_w}{\overline{\Delta}_w} = \frac{p+1}{p^\star + 1}. \tag{6.7}$$

The numerator in (6.4) can assume local negative values and this is physically consistent as it corresponds to energy backscatter, i.e. energy from the SGS scales is transferred back to the resolved scales. However, negative SGS viscosity values can numerically destabilize the simulation, especially when the sum $(\nu + \nu_{SGS})$ becomes negative. Thus, it is customary to perform some type of averaging of the numerator and denominator, generally in the directions of homogeneity. In this work, we perform two-step averaging. First, the numerator and denominator are averaged over an element to get their representative single values in each element. After this, the numerator and denominator are averaged over the homogeneous directions to get the final averaged numerator and denominator as $\langle L^d_{ij} M_{ij} \rangle$ and $\langle M_{kl} M_{kl} \rangle$, respectively. Finally, the ratio $[0.5(\langle L^d_{ij} M_{ij} \rangle / \langle M_{kl} M_{kl} \rangle)]$ is clipped to get non-negative values.

6.3. *Application to statistically stationary channel flows*

The new dynamic slip-wall model is applied to a series of statistically stationary turbulent channel flows that are homogeneous in directions parallel to the wall. The fully developed turbulent flow between the two parallel walls is separated by a distance 2δ in the z direction, where δ is the half-channel height. The flow is assumed to be periodic in the streamwise (x) and spanwise (y) directions. The simplicity of geometry and boundary conditions makes this canonical flow configuration an appealing test case, and it has been used to validate the performance of previous dynamic slip-wall models (Bose & Moin 2014; Bae *et al.* 2019).

The friction Reynolds number is set as $Re_\tau = \overline{\rho} u_\tau \delta / \mu$, with $u_\tau = \sqrt{\tau_w / \overline{\rho}}$, u_τ being the friction velocity based on the wall shear stress τ_w taken from the available DNS. The friction Reynolds number is imposed through a constant forcing in the x-momentum equation using the pressure gradient $\langle \mathrm{d}p/\mathrm{d}x \rangle = -\tau_w/\delta$. A number of WMLES studies use the constant pressure gradient as the forcing strategy in finite-volume (Yang & Bose 2017; Bae *et al.* 2019) and DG frameworks (Carton & Murman 2017; Frère *et al.* 2017; Lv *et al.* 2021). For a DNS, Quadrio, Frohnapfel & Hasegawa (2016) show that the specific choice of the forcing term, i.e. constant mass flow or constant pressure gradient, does not produce important statistical consequences and one-point statistics do not show any appreciable difference between the simulations.

The size of the computational domain is $2\pi\delta$ in the x direction and $\pi\delta$ in the y direction. The degree of polynomial p used for all the simulations presented here is 2 and the sharp modal cutoff order $p^\star$ is 1. For all the cases considered, the flow is initially evolved for at least time $20\delta/u_\tau$ units and statistics are sampled for an additional $10\delta/u_\tau$ time units. One-point statistics including the mean velocity and Reynolds shear and normal stresses are compared with the DNS of Lee & Moser (2015) and Hoyas, Oberlack & Laux (2022).

The performance of the proposed dynamic slip-wall model is validated using the cases listed in table 1, which shows the simulated Reynolds numbers and the grid resolutions in inner and outer layer units. The meshes are uniform in the streamwise, spanwise and wall-normal directions. The first element size in the wall-normal direction for all the considered cases is significantly coarser than a conventional LES mesh and the resolution is insufficient to resolve near-wall turbulent structures. As a result, none of the simulated Reynolds numbers with the grids given in table 1 are wall resolved.

Case	Re_τ	$N_x \times N_y \times N_z$	Δ_x^+	Δ_x/δ	Δ_y^+	Δ_y/δ	Δ_z^+	Δ_z/δ
DSW-2000-G1	1994.756	$8 \times 8 \times 8$	720.68	0.393	360.34	0.196	229.4	0.125
DSW-2000-G2	1994.756	$16 \times 16 \times 16$	360.34	0.196	180.17	0.098	114.7	0.0625
DSW-2000-G3	1994.756	$32 \times 32 \times 32$	180.17	0.098	90.1	0.049	57.35	0.03125
DSW-5200-G1	5185.897	$8 \times 8 \times 8$	1627.35	0.393	813.67	0.196	518	0.125
DSW-5200-G2	5185.897	$16 \times 16 \times 16$	813.67	0.196	406.84	0.098	259	0.0625
DSW-5200-G3	5185.897	$32 \times 32 \times 32$	406.84	0.098	203.42	0.049	129.5	0.03125
DSW-10000-G1	10049	$8 \times 8 \times 8$	3935	0.393	1967.52	0.196	1252.56	0.125
DSW-10000-G2	10049	$16 \times 16 \times 16$	1967.52	0.196	983.76	0.098	626.28	0.0625
DSW-10000-G3	10049	$32 \times 32 \times 32$	983.76	0.098	491.88	0.049	313.14	0.03125

Table 1. Summary of mesh parameters for the different simulated Reynolds numbers. Here, Δ_x, Δ_y and Δ_z are the effective grid sizes in the streamwise (x), spanwise (y) and wall-normal (z) directions, respectively, δ is the half-channel height and Δ_x^+, Δ_y^+ and Δ_z^+ are normalized with wall units. Here N_x, N_y and N_z represent the number of elements in the streamwise, spanwise and wall-normal directions, respectively. The number of degrees of freedom in each direction is given by $(p+1)N_x$, $(p+1)N_y$ and $(p+1)N_z$, where p is the degree of the polynomial basis. Note that the numerical experiments are labelled following the convention: [dynamic slip-wall model (DSW)]-[Re_τ]-[grid resolution].

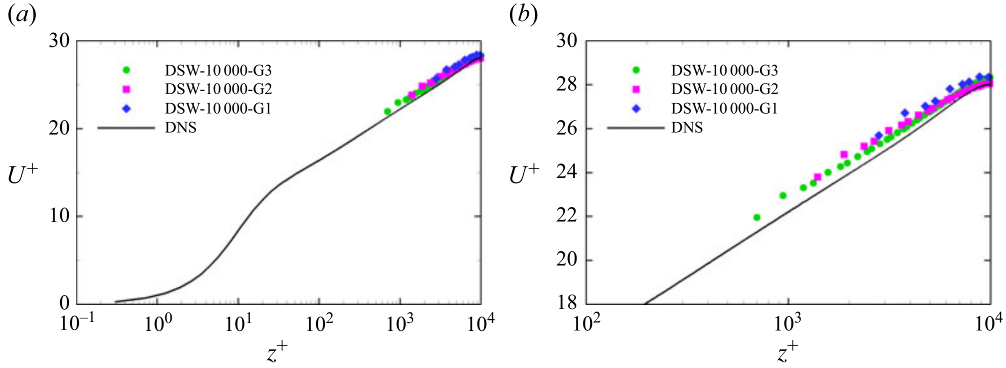

Figure 1. Grid refinement study for the proposed dynamic wall model showing comparisons between model predictions and DNS for the streamwise mean velocity at $Re_\tau \approx 10\,000$. (*a*) Classical visualization and (*b*) visualization focused on the bulk profile and the top interface of the first element.

A grid sensitivity study for channel flow at $Re_\tau \approx 10\,000$ is shown in figure 1. Starting with a coarse mesh with $8 \times 8 \times 8$ elements, the number of elements in each of the three directions is doubled at each level of refinement. This corresponds to three different coarse near-wall resolutions of $\Delta z = 0.125\delta$, 0.0625δ, and 0.03125δ, i.e. $\Delta_{z_w}^+ \approx 1253$, 626 and 313. The details of the mesh parameters are given in table 1. For all the cases, the first off-wall grid point lies in the log layer. The results are plotted starting from the second off-wall element at $(p+1)$ quadrature points in each element. It can be seen that the mean velocity for the coarsest mesh G1 has a slight positive log layer mismatch that reduces upon grid refinement. The difference between the model predictions at each of the successive grid refinement levels is less than 1 %. A grid refinement study for the other two Reynolds number cases shows a similar trend.

A comparison between the dynamic slip-wall model and the EQWM predictions with the DNS is shown in figure 2. The model predictions are obtained on grid G2 with $16 \times 16 \times 16$ elements. The slope of the mean velocity profiles obtained using the two models is similar, however, there is a slight shift between them. Both the mean velocity

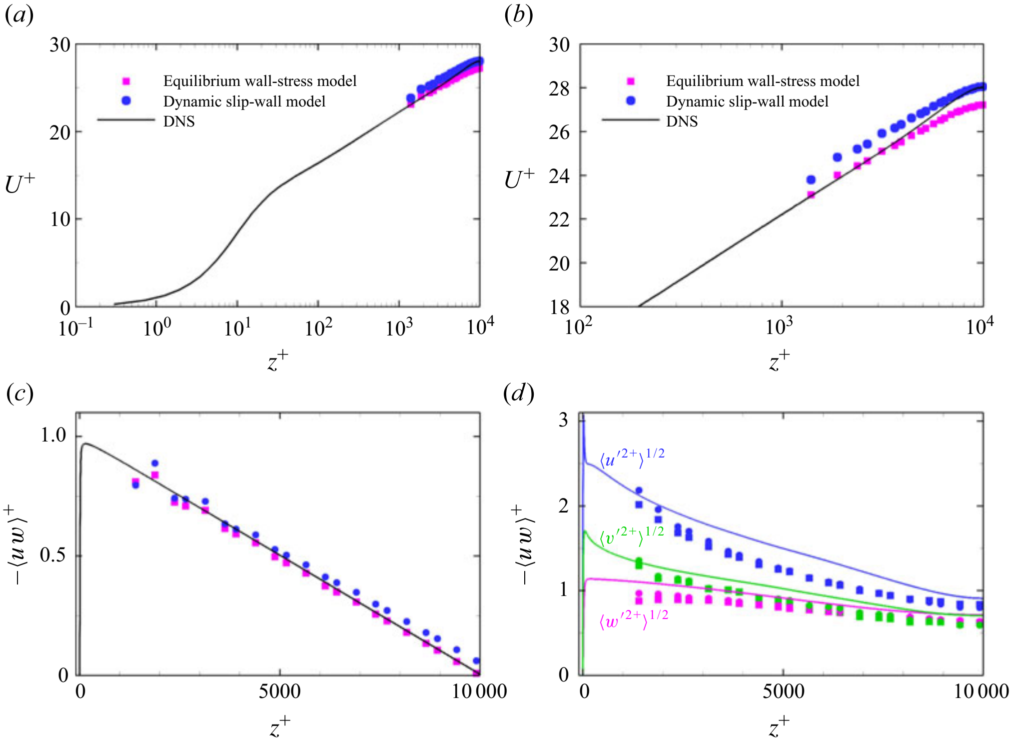

Figure 2. Comparison between the proposed dynamic slip-wall model and EQWM predictions using grid G2 with the DNS for the (*a*) full mean velocity profile, (*b*) mean velocity in the log region, (*c*) Reynolds shear stress, (*d*) root-mean-square (r.m.s.) velocity fluctuations at $Re_\tau \approx 10\,000$.

profile predictions match well with the DNS. The two model predictions for the Reynolds shear stress profiles also match the DNS well. The streamwise Reynolds stress predicted by the two models is also similar but there is a slight mismatch with the DNS. On the other hand, the spanwise and wall-normal Reynolds stress profiles obtained using the two models closely agree with the DNS.

One-point statistics on grid G2 at $Re_\tau \approx 2000, 5200$ and $10\,000$ are presented in figure 3 and compared with the available DNS. The first and second moments agree well with the DNS at the three Reynolds numbers. The model parameter C_w and mean streamwise slip velocity U_{slip} at the three Reynolds numbers and grid resolutions are plotted in figure 4. It is important to note that the slip-wall model is sensitive to the numerical implementation details, including the numerical discretization and the choice of the SGS model. Consequently, different optimal slip lengths are required for the correct prediction of the wall stress depending on the numerical set-up. As a result, the quantitative assessment of model parameters like C_w or λ with DNS is difficult. However, C_w variation with the near-wall grid resolution Δ_w^+ follows an expected trend that is qualitatively similar to that observed by Whitmore & Bose (2023) for the optimal slip length estimates, i.e. larger slip lengths on coarser near-wall grid resolutions and decay of the slip length in the limit $\Delta_w^+ \rightarrow 0$. Moreover, the slip-wall velocity trend is also consistent with the *a priori* filtering tests of Pradhan & Duraisamy (2023) using the optimal finite-element projection framework, i.e. an increase in the slip velocity with an increase in the Reynolds number on identical grids, and an increase in slip velocity at the same Reynolds number upon coarsening the grid.

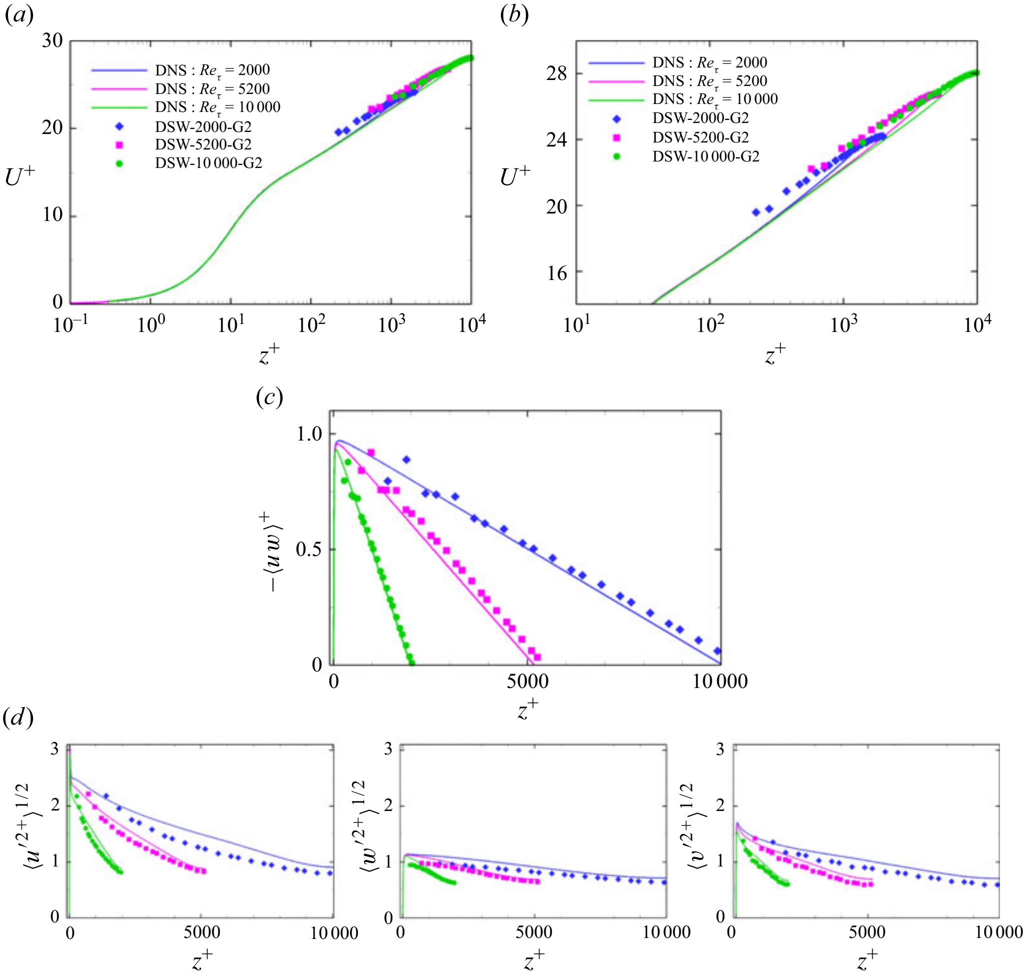

Figure 3. Comparison between DNS and proposed dynamic slip-wall model predictions using grid G2 for the (*a*) full mean velocity, (*b*) mean velocity profile in the log region, (*c*) Reynolds shear stress, (*d*) r.m.s. velocity fluctuations at $Re_\tau \approx 2000$, 5200 and 10 000.

The model parameter C_w and, hence, the slip length are found to increase as the near-wall grid is coarsened at the considered Reynolds numbers (see figure 4). The slip length modifies how momentum is transferred between the wall and the fluid. It effectively tunes the wall stress to account for near-wall turbulence effects without fully resolving the boundary layer. A larger slip length increases the velocity slip at the wall as seen in figure 4, leading to a higher velocity near the boundaries. For the considered cases, this results in the reduction of wall shear stress. For the same driving pressure gradient, this implies that more of the pressure gradient contributes to accelerating the bulk flow instead of being dissipated near the walls. As a result, the velocity profile is modified such that the mass flow rate $U_b = (1/2\delta)\int_{-\delta}^{\delta} \overline{u(z)}\mathrm{d}z$ and, hence, the bulk Reynolds number $Re_b = U_b\delta/\nu$ are found to increase for these cases as evident from the shift in mean velocity profiles relative to the DNS in figures 1 and 3. The maximum increase in the mass flow rate relative to the nominal value is about 6 % on the coarsest grid G1 and the increase reduces upon grid refinement. Figure 5 shows the change in the mass flow rate

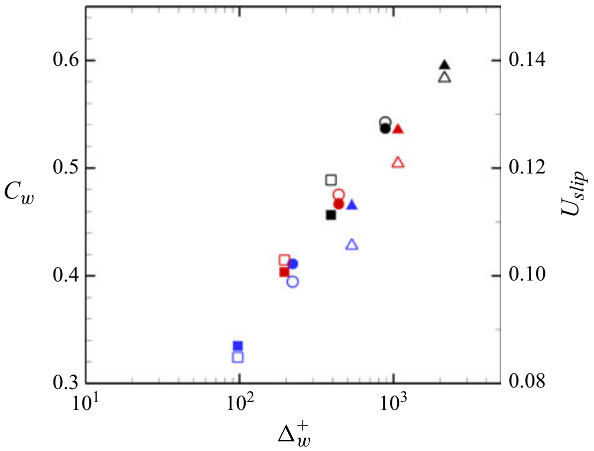

Figure 4. Slip parameter C_w (filled symbols) and streamwise slip velocity U_{slip} (unfilled symbols) as a function of near-wall grid resolution Δ_w^+ at $Re_\tau \approx 2000$ (squares), 5200 (circles) and 10 000 (deltas). Colour code: black for grid G1, red for grid G2, blue for grid G3.

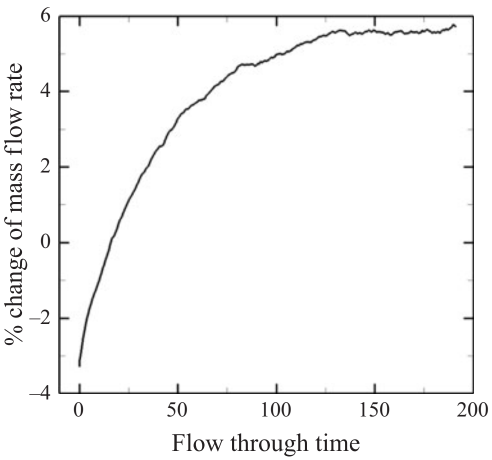

Figure 5. Change in the mass flow rate relative to the nominal value plotted as a function of the flow through time obtained at $Re_\tau \approx 2000$ on grid G2.

variation relative to its nominal value with the flow through time (L_x/U_b) at $Re_\tau \approx 2000$ on grid G2, and similar trends are observed for the other cases.

It is important to note that, the underlying assumptions for the slip condition become invalid for significantly larger near-wall grid resolutions commensurate to larger filter sizes. The shift in the mean velocity relative to the DNS is expected to increase as the near-wall grid is coarsened, as seen in figure 1. Similar observations are made in the study of Bae *et al.* (2019) using the constant pressure gradient forcing term. Note that the increase in mass flow upon coarsening the grid is also observed in LES with the no-slip boundary condition albeit on relatively finer grids than the WMLES grids.

A quantitative assessment of the dynamic slip-wall model is performed in terms of the normalized L_2 error in the streamwise mean velocity U^+ predictions with respect to the DNS for all the cases presented in table 1. The calculations exclude the first near-wall element. The normalized L_2 error is determined between the second off-wall element Δ_{2e}^+ and the half-channel height δ^+ as

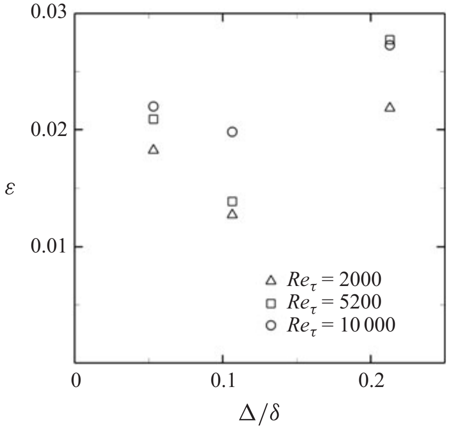

Figure 6. Normalized L_2 error, $\mathcal{E}$, in streamwise mean velocity U^+ as a function of grid resolution $\varDelta$ at $Re_\tau \approx 2000$, 5200 and 10 000.

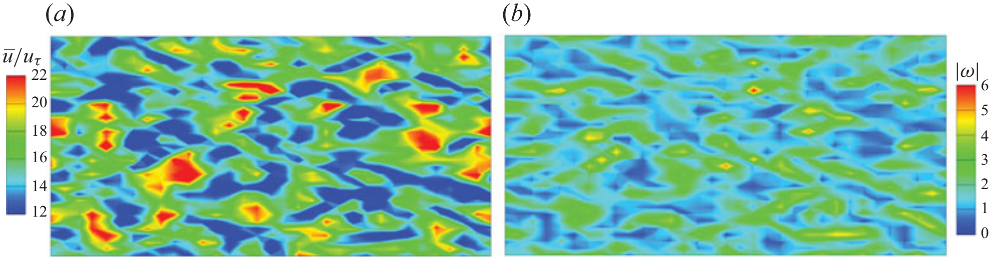

Figure 7. Snapshots of the (*a*) normalized streamwise slip velocity and (*b*) vorticity magnitude on the bottom wall obtained using the new dynamic slip-wall model at $Re_\tau \approx 10\,000$ using grid G2.

$$\mathcal{E} = \left[\frac{\int_{\varDelta_{2e}^+}^{\delta+} (U_{DSW}^+ - U_{DNS}^+)^2 \mathrm{d}z^+}{\int_{\varDelta_{2e}^+}^{\delta+} (U_{DNS}^+)^2 \mathrm{d}z^+} \right]^{1/2}. \tag{6.8}$$

Here, U_{DSW}^+ and U_{DNS}^+ represent the mean velocity obtained using the proposed dynamic slip-wall model and DNS, respectively. The error is evaluated at $(p+1)$ quadrature points within each element in the wall-normal direction z^+, and the integration for each element is performed using quadrature. The error $\mathcal{E}$ is plotted as a function of the representative grid size $\varDelta$ in figure 6. We consider $\varDelta$ based on element volume, $\varDelta = (\varDelta_x \varDelta_y \varDelta_z)^{1/3}$ with $\varDelta_x$, $\varDelta_y$ and $\varDelta_z$ taken as the effective grid sizes in the streamwise, spanwise and wall-normal directions, respectively. The L_2 error slightly increases with an increase in Reynolds number on an identical grid. However, the maximum error is less than 3 % for all the cases considered here, demonstrating the performance of the model at practically relevant Reynolds numbers on significantly under-resolved near-wall LES mesh resolutions.

Instantaneous snapshots of the streamwise slip velocity normalized by the friction velocity u_τ on the bottom wall at $Re_\tau \approx 10\,000$ employing the G2 grid is shown in figure 7(*a*). The mean slip velocity at the wall increases as the Reynolds number increases and the simulation resolves a smaller fraction of the inner layer of the boundary layer. The mean streamwise slip velocities at the wall are approximately $10.9u_\tau$, $13.9u_\tau$ and $15.35u_\tau$ for $Re_\tau \approx 2000$, 5200 and 10 000, respectively, on grid G2; the centreline velocity

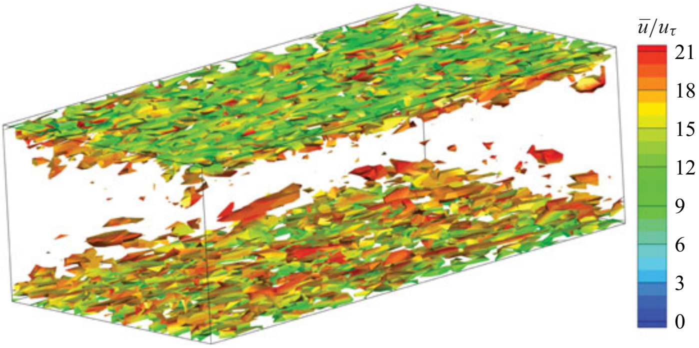

Figure 8. Isosurafces of the Q criterion coloured with normalized streamwise velocity $\overline{u}/u_\tau$ obtained using the new dynamic slip-wall model at $Re_\tau \approx 10\,000$ using grid G2.

is approximately $28u_\tau$. This behaviour is consistent with the *a priori* filtering tests of Pradhan & Duraisamy (2023) using the optimal finite-element projection framework. A snapshot of the vorticity magnitude levels on the bottom wall is also shown. The visualization of the near-wall eddies is shown in figure 8 using the Q criterion.

6.4. *Application to separated flows*

We next apply the new dynamic slip-wall model to periodic hill flows at different Reynolds numbers. The flow configuration consists of a channel flow with constrictions and forms a generic case of an internal flow separating from a curved surface. Periodic boundary conditions are applied in the streamwise (x) and spanwise (y) directions. The flow separates at the hill crest resulting in a large recirculation bubble, and it reattaches further downstream. A Reynolds number based on the bulk velocity at the crest $Re_b = \overline{\rho} U_b h/\mu$ determines the flow conditions for this case with U_b being the bulk velocity and h the hill height. The constant mass flow rate is ensured by adding a source term in the x-momentum equation. This forcing term is dynamically adjusted to provide the correct mass flow rate at the hill crest, and therefore, the correct bulk Reynolds number. The mass flux is constant to five digits of accuracy for the present computations after an initial transient.

The periodic hill case has been extensively studied over the past 15 years, both experimentally and numerically. Rapp & Manhart (2011) performed experiments in a water channel at Re_b ranging from 5600 to 37 000. Several DNS and LES (Breuer *et al.* 2009; Balakumar, Park & Pierce 2014; Diosady & Murman 2014; Gloerfelt & Cinnella 2015; Krank, Kronbichler & Wall 2018) studies have also been conducted. Many studies have also been performed to test the performance of WMLES (Balakumar *et al.* 2014; Carton & Murman 2017). The availability of high-quality data from experiments, DNS and LES makes this a good benchmark test case to evaluate the performance of the slip-wall model in the presence of separation and reattachment processes. Carton *et al.* (2018) place two-dimensional periodic hill cases at level 4 complexity in their list of benchmark test cases, which grow in complexity from level 1 to level 5. This test case is well documented and well posed with consistent DNS/LES predictions between different codes that match well with the experiments. As pointed out in Gloerfelt & Cinnella (2019), this benchmark test case has been a choice in several European projects and workshops to investigate the reliability of RANS/LES strategies.

The periodic hill flows involve massive separation on the hill's leeward sides, the length of which is about 50 % of that of the periodic segment. The principal challenge of this flow arises from the separation on the curved hill surface and the fact that the reattachment

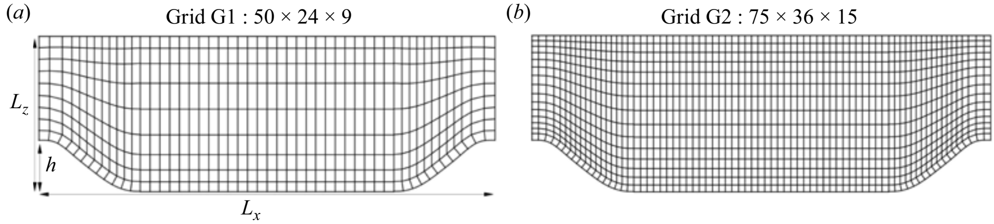

Figure 9. Coarse and fine grids used to compute the periodic hill flows.

point, and hence, the whole flow, are highly sensitive to the separation process. The flow exhibits complex dynamics, including separation, reattachment, an unsteady shear layer, a large recirculation bubble and strong acceleration on the windward wall. Resolving these delicate flow details, especially on significantly coarser grids is a challenging task. For example, in a recent work, Zhou, He & Yang (2021) developed a data-driven wall model using the feedforward neural network and training data from the WRLES of the periodic hill flows with different Reynolds numbers and hill geometries. The model shows a good performance for the turbulent channel flows at Re_τ as high as 5200. However, significant discrepancies in the mean velocity and Reynolds stress predictions are observed between their data-driven wall model and the WRLES for the periodic hill case with validation studies limited to $Re_b \approx 10\,600$.

The size of the computational domain is $L_x = 9h$, $L_y = 4.5h$ and $L_z = 3.035h$ in the streamwise (x), spanwise (y) and wall-normal (z) directions, respectively. Piecewise third-order polynomial functions give the coordinates of the curved hill, and the second hill geometry is described by the same equations with a horizontal translation (Rapp & Manhart 2011). We use two grids; a coarse grid with $50 \times 24 \times 9$ elements, i.e. $150 \times 72 \times 27$ (= 0.2916 million) degrees of freedom, and a fine grid with $75 \times 36 \times 15$ elements, i.e. $225 \times 108 \times 45$ (≈ 1.1 million) degrees of freedom. In comparison to our grids, a DNS of $Re_b \approx 10\,600$ performed by Krank *et al.* (2018) using a seventh-order DG solver, used $128 \times 64 \times 64$ elements, i.e. $896 \times 448 \times 448$ (≈ 180 million) degrees of freedom, whereas to perform an implicit LES, a mesh with $448 \times 224 \times 224$ (≈ 22.5 million) degrees of freedom was used.

The grids are approximately uniform in the streamwise and spanwise directions and a mild stretching is used in the wall-normal direction. The mesh is perpendicular to the wall in the first cell away from the wall. The effective element sizes at the hill crest, a key region for the periodic hill flow, are $\varDelta_x (= \varDelta_x^e/p) \approx 0.105h$ and $\varDelta_z (= \varDelta_z^e/p) \approx 0.093h$ for the coarse grid and $\varDelta_x \approx 0.065h$ and $\varDelta_z \approx 0.064h$ for the fine grid. Figure 9 shows the two grids used in the computations. We consider two high-Reynolds-numbers cases of $Re_b \approx 10\,600$ and 37 000 for which high-quality experimental data are available.

We first study the effect of mesh resolution on the dynamic slip-wall model predictions at $Re_b \approx 10\,600$. Wall-normal variation of the mean streamwise and wall-normal velocity profiles obtained on the coarse and fine grids is shown in figure 10, while Reynolds streamwise, wall-normal and shear stress profiles are shown in figure 11. The model predictions are compared with the experimental data and the WRLES results of Breuer *et al.* (2009) at four streamwise locations of $x = 1h$, $2h$, $4h$ and $8h$ that cover the separated as well as post-reattachment regions. The mean streamwise and wall-normal velocity profile predictions at these locations on the two grids closely match each other and they compare well with the experiments and WRLES. Note that the wall-normal velocity prediction at $x/h = 8$ is particularly sensitive to the grid refinement. This has also been observed in previous LES studies of Gloerfelt & Cinnella (2019). Notably, the WRLES

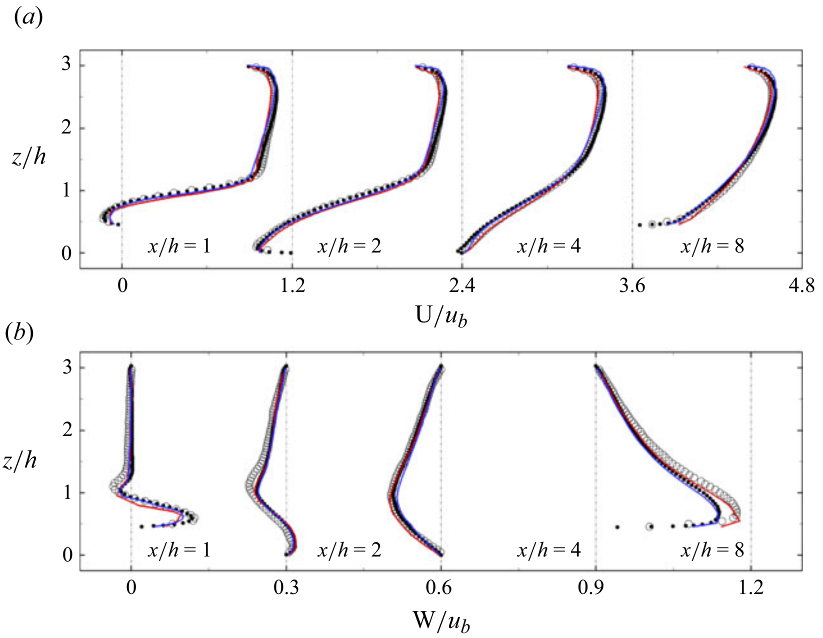

Figure 10. Effect of grid refinement on the mean velocity profiles in the streamwise (U) and vertical (W) directions at different stations for the $Re_b \approx 10\,600$ case. Red solid lines, grid G1; blue solid lines, grid G2; unfilled circles, Rapp & Manhart (2011) experiment; filled circles, WRLES by Breuer *et al.* (2009).

results for wall-normal velocity, which has a lower amplitude than the mean streamwise velocity, show discrepancies with the experiments at $x/h = 8$. Interestingly, WRLES results match well with the dynamic slip-wall predictions at this location.

The reverse flow velocities are captured well on the two grids. The Reynolds shear stress profiles on the two grids are also similar to each other and they show a good match with the experiment at the four locations. On the other hand, streamwise and wall-normal Reynolds stress profile predictions on the coarse grid follow the qualitative trend well and the predictions improve on the fine grid and get closer to the experimental data. It is to be noted that, despite the very coarse grid resolution, the agreement between the resolved part of the Reynolds shear and normal stresses with the measurement is reasonably good.

The periodic hill flow is then computed at a higher Reynolds number of $Re_b = 37\,000$ using the fine grid and comparisons between the new dynamic slip-wall model and the EQWM predictions for the mean velocities and Reynolds stresses are shown in figures 12 and 13, respectively. The EQWM significantly underpredicts the separation and shows a faster recovery and the mean streamwise and wall-normal velocity profiles in the separated regions show a significant mismatch with the experiments. On the other hand, the dynamic slip-wall model accurately captures the separation and shows an excellent match with the experiments for the mean velocities at the four locations in figure 12. A discrepancy is observed for the wall-normal velocity at $x/h = 8$ similar to the $Re_b \approx 10\,600$ case, which is consistent with the study of Gloerfelt & Cinnella (2019). The Reynolds shear stress profiles predicted by the dynamic slip-wall model also closely agree with the experiments whereas the EQWM model predictions show a considerable mismatch. This is also the case for the streamwise Reynolds stress profiles. However, the dynamic slip-wall model predictions for the wall-normal Reynolds stress show some discrepancies and overpredict the levels found in the experiments. This is again consistent with the LES studies of

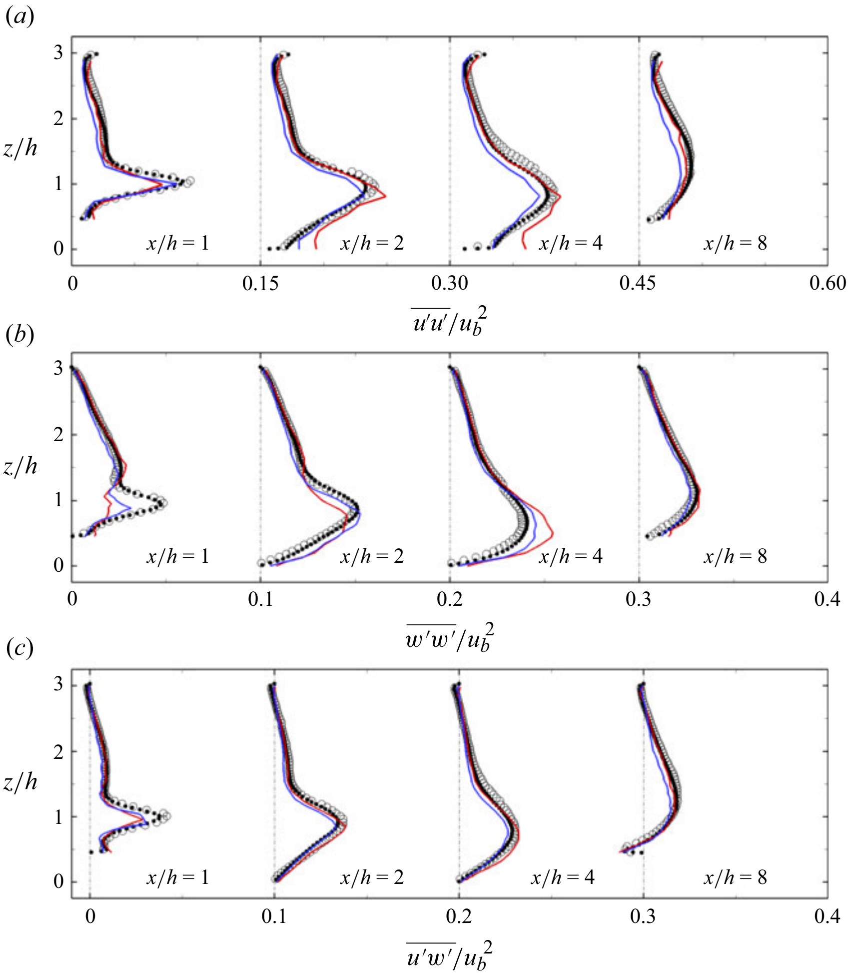

Figure 11. Effect of grid refinement on the profiles of Reynolds stresses in the streamwise (U) and vertical (W) directions at different stations for the $Re_b \approx 10\,600$ case. Red solid lines, EQWM; red solid lines, grid G1; blue solid lines, grid G2; unfilled circles, Rapp & Manhart (2011); experiment; filled circles, WRLES by Breuer *et al.* (2009).

Gloerfelt & Cinnella (2019) that showed dramatic overprediction for the wall-normal Reynolds stresses while getting a good match for the other Reynolds stress components. Overall, the dynamic slip-wall model predictions are considerably better than the EQWM.

Figure 14 plots the variation of λ-normalized slip parameter C_w, i.e. $C_{w,\lambda}$, as a function of the slip-velocity-based Reynolds number Re_{slip} and λ for the two Reynolds numbers of $Re_b \approx 10\,600$ and 37 000 obtained on grids G1 and G2. The curves for $C_{w,\lambda}$ are found to collapse as a function of Re_{slip} for the two grid resolutions, and the universal scaling relationship discovered in Pradhan & Duraisamy (2023) for turbulent channel flows using an *a priori* analysis is found to remain valid for these separated flows as well in the *posteriori* computations. The parameter $C_{w,\lambda}$ follows the expected trend; assumes lower values at the lower Reynolds number and coarser near-wall grid resolutions and decays as the near-wall grid is coarsened or the Reynolds number is decreased. The streamwise variation of the slip parameter C_w is shown in figure 15 and it also follows the expected trend at the two Reynolds numbers and grid resolutions. Variations in C_w along the

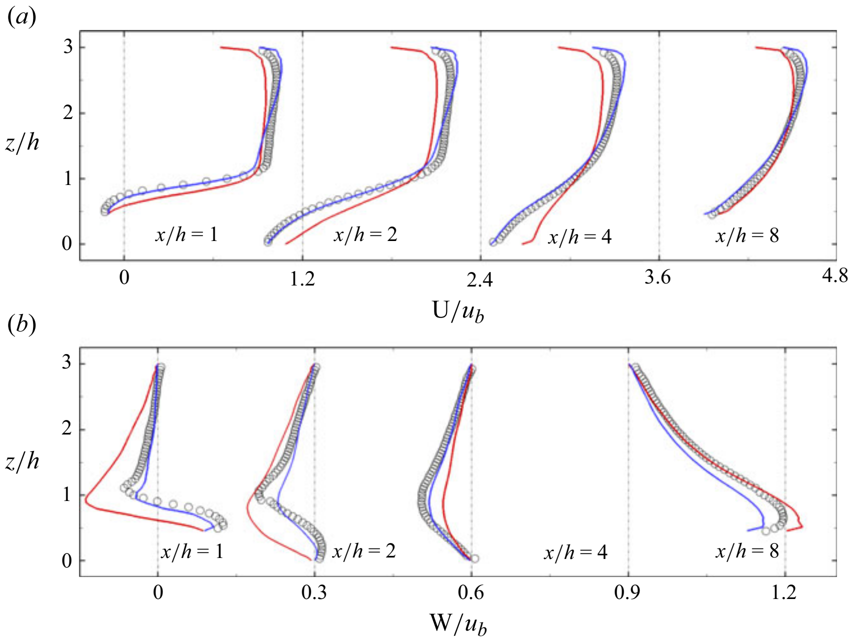

Figure 12. Mean velocity profiles in the streamwise (U) and vertical (W) directions at different stations for the $Re_b \approx 37\,000$ case. Red solid lines, EQWM; blue solid lines, dynamic slip-wall model; unfilled circles, Rapp & Manhart (2011) experiment.

streamwise direction are also observed for these cases. The sudden peaks at the start of the hill and at $x/h \approx 7$ for the high-Reynolds-number case of $Re_b \approx 37\,000$ are indicative of the unphysical effects due to the coarse grid resolution and these peaks vanish on the fine grid G2.

The streamwise distributions of the mean streamwise slip-wall velocity at $Re_b \approx 10\,600$ and 37 000 obtained on the fine grid G2 are shown in figure 16. The slip velocity U_{slip} for the two cases changes the sign near the separation point, remains negative in the separation bubble and reverses the sign near the reattachment location. For the $Re_b \approx 10\,600$ case, the locations where the slip velocity changes the sign closely match the experimental measurements and WRLES results for the separation and reattachment points at $x/h \approx 0.2$ and $x/h \approx 4.6$, respectively. As indicated by the negative values of the slip velocity, the separation region slightly reduces in size at the higher Reynolds case, which is physically consistent.

7. Conclusion

Several strategies have been proposed to bypass the stringent near-wall grid resolution requirement for performing LES of high-Reynolds-number flows in the presence of solid walls. In this work, we focus on the slip-wall modelling approach – originally proposed by Bose & Moin (2014) – and replace the conventional no-slip velocity boundary condition with slip velocities at the wall. The major objective is to accurately capture the mean flow characteristics at Reynolds numbers of practical relevance using a significantly coarse near-wall LES mesh, and do so in a robust manner.

We present a new formulation of a dynamic slip-wall model that is consistent with the DG framework and is tightly integrated with DG operators. The model coefficients of the

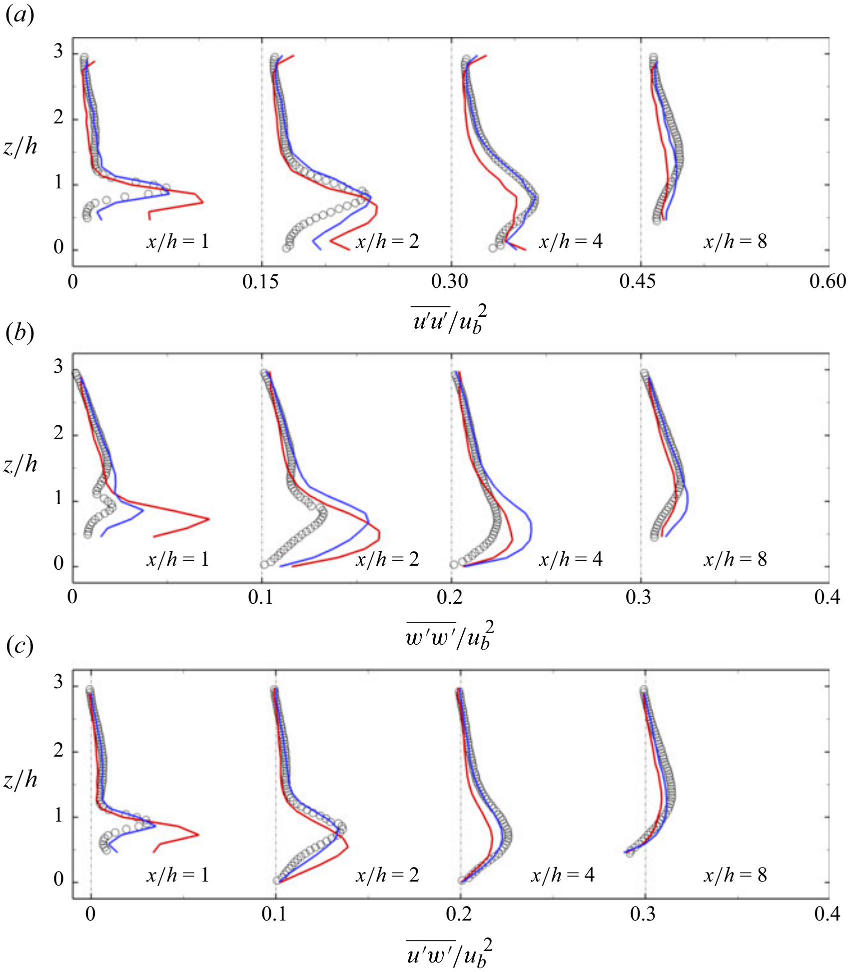

Figure 13. Profiles of Reynolds stresses in the streamwise (U) and vertical (W) directions at different stations for the $Re_b \approx 37\,000$ case. Red solid lines, EQWM; blue solid lines, dynamic slip-wall model; unfilled circles, Rapp & Manhart (2011) experiment.

modified slip-wall model of Pradhan & Duraisamy (2023) are based on *a priori* estimates obtained using an optimal finite-element projection framework. Here, we propose a dynamic modelling procedure to compute the scaling parameter λ for the slip-wall model coefficient C_w. The dynamic part of the model is based on a modified form of the Germano identity and coupled with the DSM. The level of under-resolution is represented by a slip Reynolds number and the proposed model attempts to also incorporate the effects of the numerical discretization and the SGS model.

The canonical case of a statistically stationary turbulent channel flow is first used to validate the new dynamic slip-wall model. The model predictions are compared with the available DNS data at three Reynolds numbers of $Re_\tau \approx 2000$, 5200 and 10 000. Grid independence studies are performed at these Reynolds numbers by considering significantly under-resolved LES meshes with streamwise, spanwise and wall-normal grid resolutions corresponding to $\Delta_x \simeq 0.1 - 0.4\delta$, $\Delta_y \simeq 0.05 - 0.2\delta$ and $\Delta_z \simeq 0.03 - 0.125\delta$, respectively. These mesh resolutions are significantly coarser than the WMLES mesh

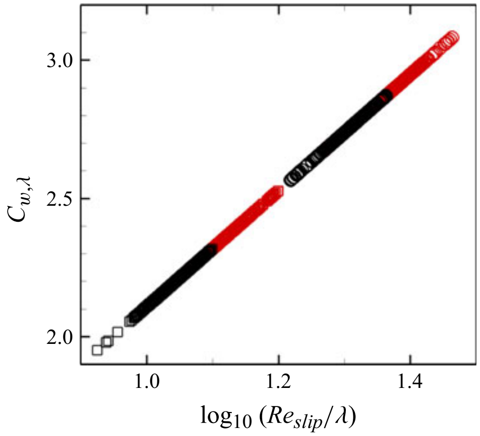

Figure 14. Plot of λ-normalized slip parameter C_w, i.e. $C_{w,\lambda}$, as a function of Re_{slip} and λ at $Re_b \approx 10\,600$ (squares) and $Re_b \approx 37\,000$ (circles). CColour code: black for grid G1; red for grid G2.

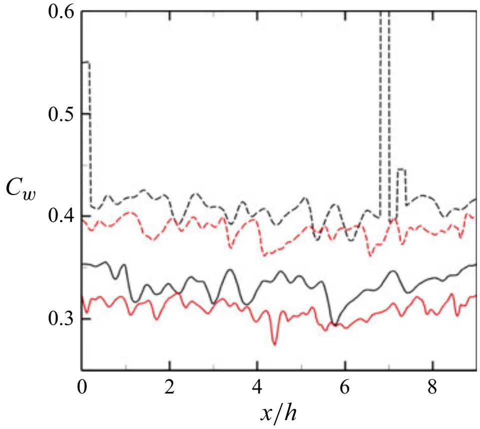

Figure 15. Streamwise distribution of the slip parameter C_w at $Re_b \approx 10\,600$ (solid lines) and $Re_b \approx 37\,000$ (dashed lines) obtained on grid G1 (black lines) and grid G2 (red lines).

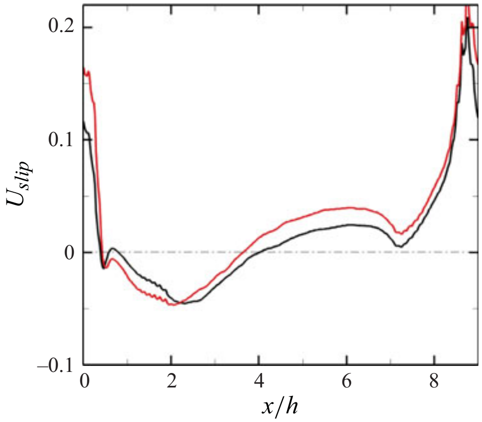

Figure 16. Streamwise distribution of the slip velocity U_{slip} at $Re_b \approx 10\,600$ (black line) and $Re_b \approx 37\,000$ (red line) obtained on grid G2.

recommendations of Larsson *et al.* (2016) corresponding to $\varDelta_x \simeq 0.08\delta$, $\varDelta_y \simeq 0.05\delta$ and $\varDelta_z \simeq 0.01-0.05\delta$. Mean velocity profiles show an excellent match with the DNS at the considered Reynolds numbers on all the grids with an L_2 error less than 3 % for all the cases. Reynolds shear and normal stress profiles resolved on the significantly coarse grids also show excellent agreement with the DNS. The model performance is shown to be similar to that of the EQWM, which is known to predict the equilibrium wall-bounded flows without separation accurately. This is a considerable improvement over the dynamic slip-wall model of Bae *et al.* (2019) that shows a significant log layer mismatch at similar Reynolds numbers but on comparatively finer grid resolutions.

The model performance is evaluated in flow separation and reattachment over periodic hills at Reynolds numbers of $Re_b \approx 10\,600$ and 37 000 using two different grid resolutions. The meshes used for the computations are significantly coarser than the conventional LES meshes, e.g. the fine mesh used here has about 20 times fewer degrees of freedom than the implicit LES performed by Krank *et al.* (2018). The streamwise and wall-normal mean velocity profile predictions obtained using the dynamic slip-wall model on the two grids compare well with the experimental data in the separated and post-reattachment flow regions at $Re_b \approx 10\,600$. Reynolds shear stress predictions obtained using the two grids also match very well with experiments at different streamwise locations. However, the Reynolds normal stresses are better predicted on the fine grid. Computations at $Re_b \approx 37\,000$ using the fine grid show that the dynamic slip-wall model predictions for the mean velocity profiles agree well with the experiments. The Reynolds shear stress profiles are also in excellent agreement with the experiments, with some discrepancies in the Reynolds normal stress predictions. On the other hand, EQWM for this case shows significant discrepancies with the experimental data for the mean velocities as well as Reynolds shear and normal stresses.

The new model contains parameters like $C_{w,\lambda}$, C_{wR} and $\varDelta_R$ that are empirically established, but the model does not assume the state of a boundary layer. It is important to note that the main purpose of a slip-wall model is similar to that of a traditional wall-stress model, i.e. accurate estimation of wall shear stress. Achieving this goal without prior assumptions regarding the state of the boundary layer or embedded empirical parameters is an outstanding challenge. Moreover, the instantaneous velocity field is intertwined with the effects of the LES grid resolution and Reynolds number for a given numerical discretization and SGS model as discussed in Bae *et al.* (2019). The modelling choices made in this work are consistent with the observations of Pradhan & Duraisamy (2023) and the works of Bose & Moin (2014), Bae *et al.* (2019). The empirical parameters in the proposed model, especially $C_{w,\lambda}$, provide an explicit reference to how the near-wall flow should behave at different near-wall grid resolutions and Reynolds numbers. The model is found to be somewhat insensitive to the parameters C_{wR} and $\varDelta_R$ in their plausible range for the considered cases, which includes the smooth body-separated flows with separation and reattachment.

The new model can consistently predict mean velocity and Reynolds shear and normal stress profiles for the equilibrium as well as separated flows at high Reynolds numbers using significantly coarse near-wall LES meshes. The model performs at a computational cost similar to the EQWM, which is the cheapest state-of-the-art WMLES strategy. In the authors’ opinion, the excellent performance of the model may be attributed to the integration of the optimal finite-element projection framework used to obtain the slip-wall parameters with the consistent dynamic procedures for the SGS and slip-wall modelling coupled with the DG framework. This work is a step towards making the slip-wall model a viable computing tool for predicting complex engineering flows, and further evaluations are required.

While the present work demonstrates the implementation and validation of the dynamic slip-wall model within a DG framework, we emphasize that the fundamental approach is not inherently tied to DG methods. The essential requirement is a rigorous coarse graining or scale separation operator, which can be provided by various numerical frameworks including finite-element methods, variational multiscale approaches or projection-based methods. For finite-volume and finite difference techniques, while the implementation is less straightforward, agglomeration-based techniques (see, e.g. Gravemeier 2006) can provide viable pathways. Changing the numerical framework (for instance, to continuous finite elements) would necessitate recalibration of the base parameters, along with a redefinition of the length scales. This requirement stems from our fundamental observation that subgrid and wall models cannot be decoupled from the underlying numerical method due to the strong interactions between unresolved and coarsely resolved dynamics.

Acknowledgement. This research was funded by NASA under the project ‘Scale-resolving turbulence simulations through adaptive high-order discretizations and data-enabled model refinements’, grant number 80NSSC18M0149 (technical monitor: Dr Gary Coleman). We acknowledge Professor Krzysztof Fidkowski, Dr Gary Coleman and Dr Aniruddhe Pradhan for their valuable discussions.

Declaration of interests. The authors report no conflict of interest.

Appendix A. Sharp modal cutoff filter implementation

The implementation of the sharp modal cutoff filter is a three-step process: transforming the nodal solution coefficients to a hierarchical modal representation, applying a filter on the modal coefficients and then transforming back into the nodal representation. Let us denote the nodal solution coefficients as u_j, the nodal basis functions as ϕ_j, the modal solution coefficients as b_j and the modal basis functions as ψ_j. Then, we can write the approximation u_h to any flow variable u in an element as

$$u \approx u_h = \sum_{j=1}^{p+1} u_j \phi_j = \sum_{j=1}^{p+1} b_j \psi_j \,. \tag{A1}$$

Multiplying the above equation by ψ_i and integrating over the standard element, we get

$$\sum_{j=1}^{p+1} C_{ij} u_j = \sum_{j=1}^{p+1} M_{ij} b_j \tag{A2}$$

or in matrix and vector form, we can write

$$[C]\boldsymbol{u} = [M]\boldsymbol{b}\,. \tag{A3}$$

Here, the modal mass matrix [M] is given by

$$[M] = M_{ij} = \int_{\Omega_k} \psi_i \psi_j \, \mathrm{d}x. \tag{A4}$$

The mixed mass matrix [C] is given by

$$[C] = C_{ij} = \int_{\Omega_k} \psi_i \phi_j \, \mathrm{d}x. \tag{A5}$$

Using (A3), we can obtain the modal solution coefficients, $\boldsymbol{b}$, from the nodal solution coefficients $\boldsymbol{u}$ by inverting the modal mass matrix [M], i.e.

$$\boldsymbol{b} = [M]^{-1}[C]\boldsymbol{u}. \tag{A6}$$

Now that the hierarchical modal basis coefficients have been obtained, a square filter matrix, [F], can be applied as a matrix-vector product, i.e.

$$\widehat{\boldsymbol{b}} = [F]\boldsymbol{b}, \tag{A7}$$

where $\widehat{\boldsymbol{b}}$ are the filtered modal solution coefficients. The sharp cutoff filter matrix $[F]$ is diagonal with its entries being 0 or 1. If all entries are 1 giving the identity matrix, the filtering operation returns the original solution. To obtain a cutoff filter of order $(p^\star + 1)$, all diagonal entries of the filter matrix are 1 up to and including the $(p^\star + 1)$ diagonal entry with the rest of the entries 0. The last step in the modal decomposition filtering procedure is to transform the filtered modal coefficients back to nodal basis coefficients to give the filtered nodal solution. This reverse transformation can be performed as follows :

$$\widehat{\boldsymbol{u}} = [C]^{-1}[M]\widehat{\boldsymbol{b}}, \tag{A8}$$

$$= [C]^{-1}[M][F]\boldsymbol{b} \quad \text{by (A7)}, \tag{A9}$$

$$= [C]^{-1}[M][F][M]^{-1}[C]\boldsymbol{u} \quad \text{by (A6)}. \tag{A10}$$

Let

$$[B] = [M]^{-1}[C] \quad \text{and} \quad \widehat{[F]} = [B]^{-1}[F][B]. \tag{A11}$$

We can then write the final filtered nodal solution coefficients as

$$\widehat{\boldsymbol{u}} = \widehat{[F]}\boldsymbol{u}. \tag{A12}$$

The final filter matrix $\widehat{[F]}$ can be assembled as a pre-processing step as it does not have a dependence on the solution.

The sharp modal filter is first tested in a one-dimensional DG set-up. The objective is to find a best fit for the function $u(x) = cos(2x) + 0.3sin(8x)$. The degree of the Lagrange basis function is set to $p = 3$, and the sharp modal cutoff filter is tested for $p^\star = 0, 1, 2$ and 3. The number of elements used is 10 with four quadrature points on each element, and the results are presented in figure 17. The analytical solution is plotted for the domain $[-\pi, \pi]$. The nodal DG solution with $p = 3$ matches closely with the analytical solution, and the jumps at the element approximation denote the discontinuous nature of the approximation. The sharp modal cutoff filter with $p^\star = 3$ does not affect the solution and the results are identical to the original solution. On the other hand, lower cutoff orders of $p^\star = 2$, 1 and 0 result in a piecewise quadratic, linear and constant solution, respectively.

The modal sharp cutoff filter in its one-dimensional form discussed above is extended to three dimensions in a tensor product fashion and applied before every RK3-TVD step in our in-house DG code. The effect of the test filtering operation using the modal sharp cutoff filter on the normalized instantaneous streamwise velocity $\overline{u}/u_\delta$ is shown in figure 18. The degree of polynomial used is $p = 3$ and results are shown for the $Re_\tau \approx 544$ case with filter orders of $p^\star = 3, 2, 1$ and 0. The snapshots of $\overline{u}/u_\tau$ show the loss of information and decrease in resolution of the flow field as the filter cutoff order is reduced.

Appendix B. Wall-resolved LES at $Re_\tau \approx 544$

A WRLES of the turbulent channel flow is performed at $Re_\tau \approx 544$ using the DSM as the SGS model to verify our in-house DG solver. The mesh size is 36 × 30 × 24 elements in the streamwise, spanwise and wall-normal directions, respectively. The grid is uniform in the streamwise and spanwise directions and it is geometrically stretched in the wall-normal direction with a stretching ratio of 1.2. The effective grid sizes in each direction in wall units are $\Delta_x^+ \approx 38$, $\Delta_y^+ \approx 19$ and Δ_z^+ at the wall is $\Delta_{z_w}^+ \approx 4.5$ and at the channel

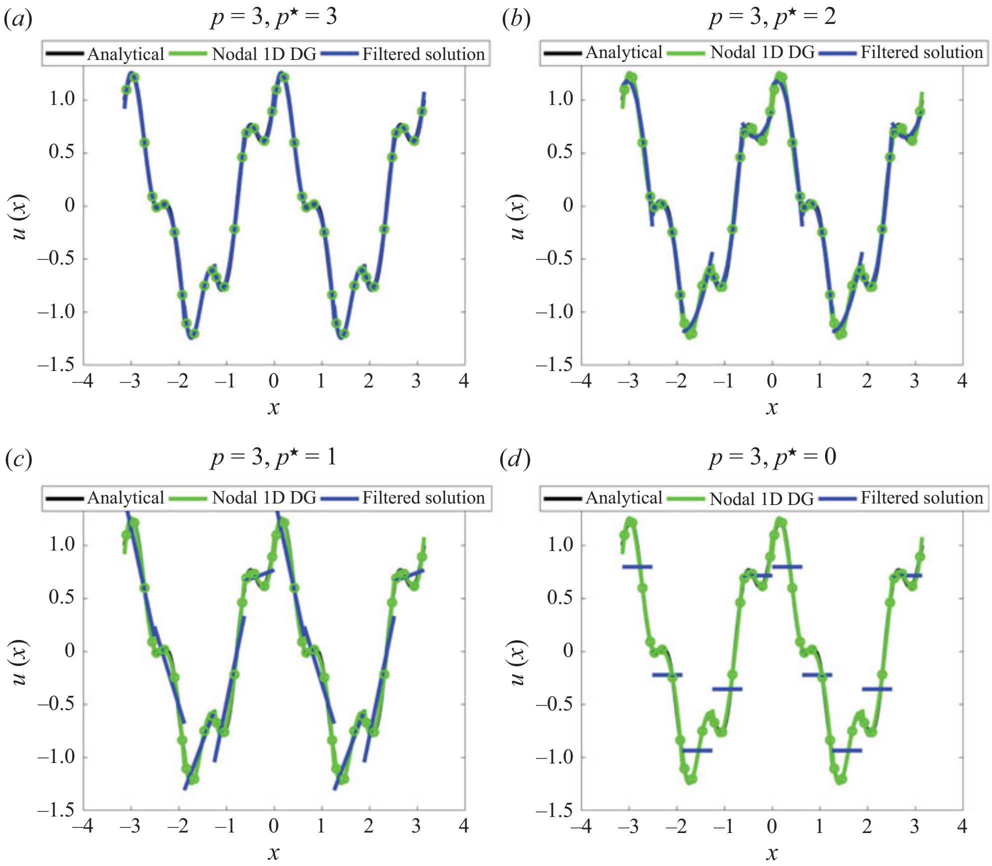

Figure 17. Comparisons of analytical solution for a function $u(x) = cos(2x) + 0.3sin(8x)$ in the range $[-\pi, \pi]$ with the best fit obtained using one-dimensional nodal DG employing 10 elements and $p = 3$ along with filtered solutions for $p^{\star} = 0$, 1, 2 and 3. Unfilled green circles indicate the quadrature points within each element.

centre is $\Delta^{+}_{z_c} \approx 32.2$. The grid resolution is based on the recommendation of Bose & Moin (2014) for a WRLES, i.e. $\Delta^{+}_{x} \lesssim 50$, $\Delta^{+}_{y} \lesssim 30$ and $\Delta^{+}_{z_w} \sim O(1)$. In comparison, the grid resolution of the available DNS (Lee & Moser 2015) is $\Delta^{+}_{x} \approx 8.9$, $\Delta^{+}_{y} \approx 5$, $\Delta^{+}_{z_w} \approx 0.019$ and $\Delta^{+}_{z_c} \approx 4.5$. Please note that, the effective grid sizes Δ_x, Δ_y and Δ_z for the finite-element grid are defined as $\Delta_x = \Delta^{e}_{x}/p$, Δ^{e}_{y}/p and Δ^{e}_{z}/p, respectively. The quantities Δ^{e}_{x}, Δ^{e}_{y} and Δ^{e}_{z} represent the actual element sizes in the finite-element mesh.

The instantaneous streamwise velocities $\overline{u}$ normalized with u_τ for the WRLES in the xz plane are shown in figure 19(*a*). The solution is reasonably resolved. Snapshots of the vorticity magnitude on the bottom wall are shown in figure 19(*b*). On the other hand, figure 19(*c*) shows the isometric view of the isosurfaces of the Q criterion to visualize the near-wall eddies.

The wall-normal variation of the mean Smagorinsky coefficient $\langle C_s \rangle$ along with mean velocity and Reynolds shear and normal stresses for the WRLES compared with the DNS is shown in figure 20. The Smagorinsky coefficient C_s for the DSM assumes a value of zero at the wall as L^{d}_{ij} in (6.4) is equivalently zero at the wall owing to the no-slip velocity boundary condition. It gradually increases in the viscous sublayer before reaching a value of about 0.12 in the log layer at about $z^{+} \approx 60$ after which it remains close to $0.1 - 0.12$

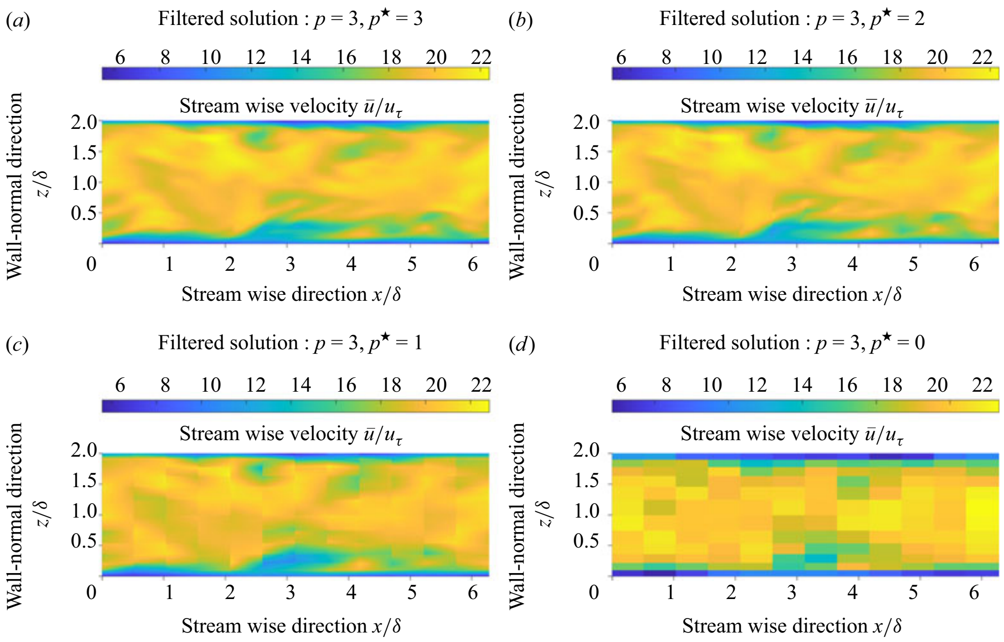

Figure 18. Snapshots of normalized streamwise velocity in the xz plane passing midway through the spanwise domain dimension with $p^\star = 3$, 2, 1 and 0 showing the effects of the test filtering operation at $Re_\tau \approx 544$.

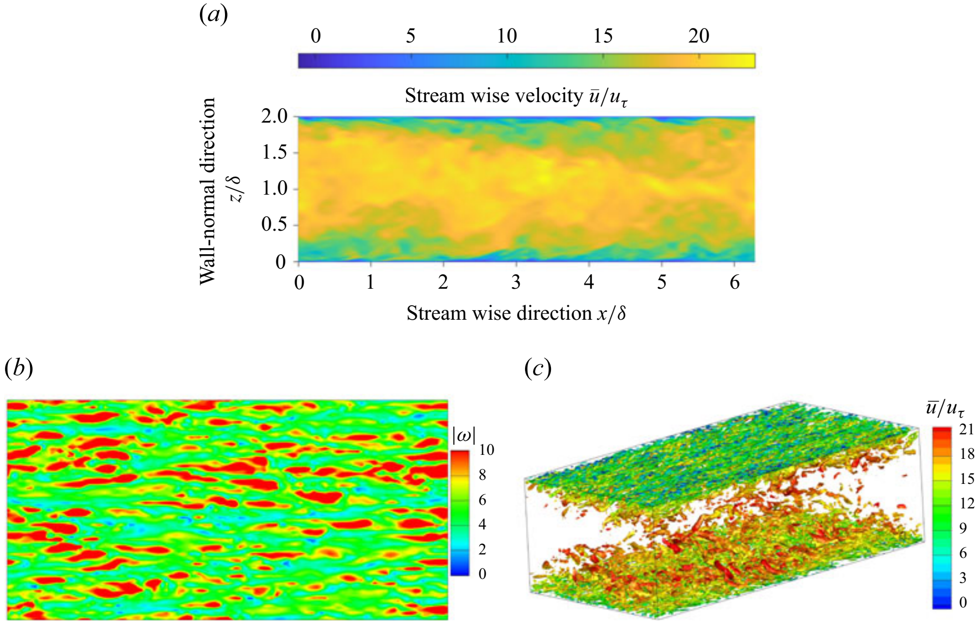

Figure 19. (*a*) Snapshot of normalized streamwise velocity in the xz plane passing midway through the spanwise dimension, (*b*) snapshot of the vorticity magnitude on the bottom wall and (*c*) isosurface of the Q criterion coloured with normalized streamwise velocity $\bar{u}/u_\tau$ for a WRLES at $Re_\tau \approx 544$ obtained using the DSM SGS model.

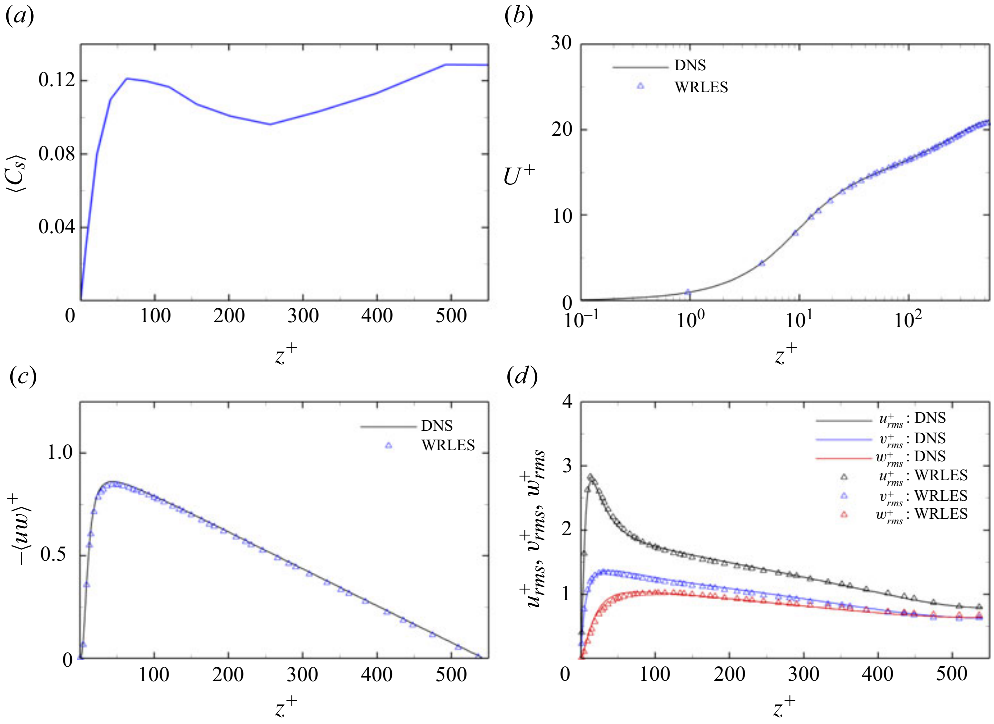

Figure 20. Wall-normal variation of the (*a*) mean Smagorinsky coefficient $\langle C_s \rangle$, (*b*) mean velocity, (*c*) Reynolds shear stress and (*d*) r.m.s. velocity fluctuations for a WRLES employing DSM as the SGS models compared with the DNS at $Re_\tau \approx 544$.

till the half-channel height δ^+. The mean velocity and Reynolds shear and normal stress profiles obtained using the WRLES are nearly identical to the DNS data.

Appendix C. Sensitivity analysis

The proposed dynamic slip-wall model involves two model parameters, namely C_{wR} and Δ_R. The definition of the filter operation fixes the value of Δ_R, which is the ratio of the test filter width to the grid filter width. We used a value for Δ_R as recommended by Brazell *et al.* (2015). Numerical experiments using different values for Δ_R in the plausible range of $\Delta_R = [1, 2]$ for $p = 2$ and $p^\star = 1$ resulted in negligible differences in the results and these observations are similar to those made by Bae *et al.* (2019) for their dynamic slip-wall model. On the other hand, the parameter C_{wR} comes into the picture because of the use of different values of the model coefficient C_w at the test filter and grid filter levels. The sensitivity to C_{wR} is tested for values in the plausible range $C_{wR} = [1, 2]$. Results for the two extreme values in this range, i.e. $C_{wR} = 1$ and 2, are shown in figure 21 for the $Re_\tau \approx 10\,000$ case obtained using grid G2. The effect of C_{wR} on the mean velocity and Reynolds stress predictions is also found to be negligible and the results are almost identical. This suggests that the model coefficient C_w can be taken to be the same at the test- and grid-filtered levels, which is the general practice (Bose & Moin 2014; Bae *et al.* 2019).

Appendix D. Computational cost

The simulations were performed on NASA's Pleiades Supercomputer on the Broadwell compute nodes consisting of E5-2680v4 Intel Xeon processors at 2.4 GHz. For the channel

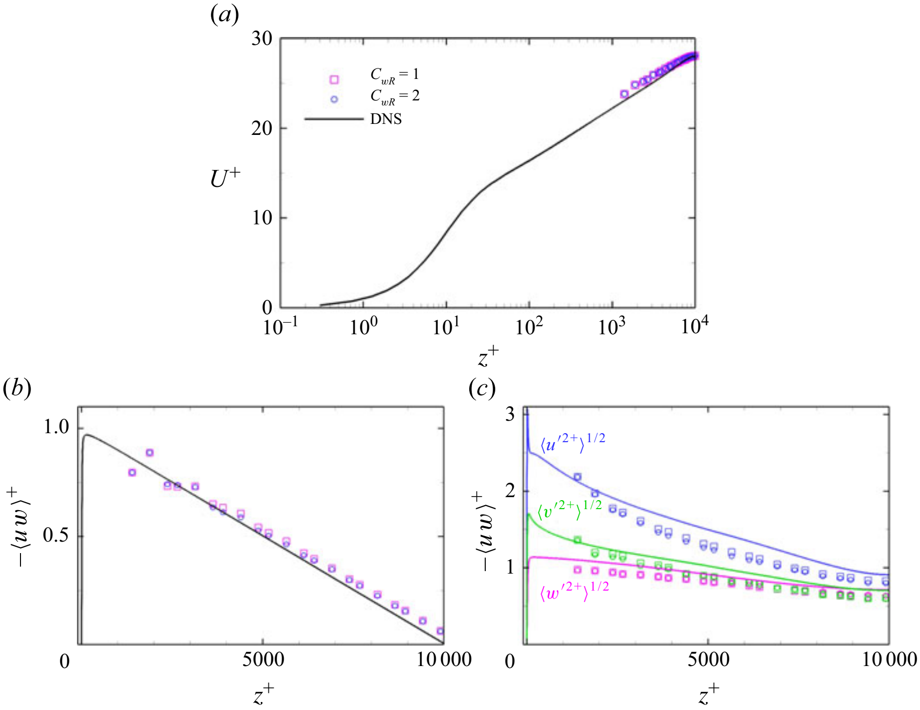

Figure 21. Effect of the parameter C_{wR} values on the proposed dynamic wall model predictions for the case DSW-10000-G2 along with DNS comparisons for the (*a*) mean velocity, (*b*) Reynolds shear stress and (*c*) r.m.s. velocity fluctuations.

flow computations on the finest mesh G3 consisting of 32 × 32 × 32 elements with about 0.885 million degrees of freedom, the dynamic slip-wall model takes about 0.135 s of wall time per time step on 512 processors. For the $Re_\tau \approx 10\,000$ case, the dynamic slip-wall model requires a wall time of about 11.8 mins for a single flow through $(= L_x/U_b)$ on the grid G3. On the other hand, for the periodic hill cases using the fine grid consisting of 75 × 36 × 15 elements with about 1.1 million degrees of freedom, the wall time required by the dynamic slip-wall model per time step is approximately 0.088s on 3330 processors. For the $Re_b = 37\,000$ case, the wall time required for a single flow through is about 22 mins. The EQWM requires a similar time per time step as that of the dynamic slip-wall model for the channel flow and periodic hill cases on identical grids. On the other hand, a static slip-wall model using an arbitrary constant value of the slip length takes about 1 % less time per time step for the channel flow on the G3 mesh and about 7 % less time per time step for the periodic hill case on the G2 grid in comparison to the dynamic slip-wall model on an identical number of processors.

REFERENCES

AGRAWAL, R., BOSE, S.T. & MOIN, P. 2024 Non-equilibrium wall model for large eddy simulations of complex flows exhibiting turbulent smooth body separation. *Phys. Rev. Fluids* **9** (12), 124603.

AGRAWAL, R., WHITMORE, M.P., GRIFFIN, K.P., BOSE, S.T. & MOIN, P. 2022 Non-Boussinesq subgrid-scale model with dynamic tensorial coefficients. *Phys. Rev. Fluids* **7** (7), 074602.

BAE, H.J., LOZANO-DURÁN, A., BOSE, S.T. & MOIN, P. 2019 Dynamic slip wall model for large-eddy simulation. *J. Fluid Mech.* **859**, 400–432.

BALAKUMAR, P., PARK, G.I. & PIERCE, B. 2014 DNS, LES, and wall-modeled LES of separating flow over periodic hills. In *Proceedings of the Summer Program*, pp. 407–415. Stanford University.

Balaras, E., Benocci, C. & Piomelli, U. 1996 Two-layer approximate boundary conditions for large-eddy simulations. *AIAA J.* **34** (6), 1111–1119.

Bassi, F. & Rebay, S. 2000 GMRES discontinuous Galerkin solution of the compressible Navier–Stokes equations. In *Discontinuous Galerkin Methods: Theory, Computation and Applications*, pp. 197–208. Springer.

Bodart, J. & Larsson, J. 2011 *Wall-Modeled Large Eddy Simulation in Complex Geometries with Application to High-Lift Devices*. Annual Research Briefs, Center for Turbulence Research, Stanford University.

Bose, S.T. & Moin, P. 2014 A dynamic slip boundary condition for wall-modeled large-eddy simulation. *Phys. Fluids* **26** (1), 015104.

Bose, S.T. & Park, G.I. 2018 Wall-modeled large-eddy simulation for complex turbulent flows. *Annu. Rev. Fluid Mech.* **50** (1), 535–561.

Brazell, M.J., Brazell, M.J., Stoellinger, M.K. & Mavriplis, D.J. 2015 Using LES in a discontinuous Galerkin method with constant and dynamic SGS models. In *Proceedings of the 53rd AIAA Aerospace Sciences Meeting*, pp. 0060.

Breuer, M., Peller, N., Rapp, C. & Manhart, M. 2009 Flow over periodic hills–numerical and experimental study in a wide range of Reynolds numbers. *Comput. Fluids* **38** (2), 433–457.

Cabot, W. & Moin, P. 2000 Approximate wall boundary conditions in the large-eddy simulation of high Reynolds number flow. *Flow Turbul. Combust.* **63** (1/4), 269–291.

Carton de Wiart, C., Larsson, J. & Murman, S. 2018 Validation of WMLES on a periodic channel flow featuring adverse/favorable pressure gradients. In *Proceedings of the Tenth International Conference on Computational Fluid Dynamics (ICCFD10)*. vol. 355.

Carton de Wiart, C. & S.M., Murman 2017 Assessment of wall-modeled LES strategies within a discontinuous-Galerkin spectral-element framework. In *Proceedings of the 55th AIAA Aerospace Sciences Meeting*, pp. 1223.

Cheng, W., Pullin, D.I. & Samtaney, R. 2015 Large-eddy simulation of separation and reattachment of a flat plate turbulent boundary layer. *J. Fluid Mech.* **785**, 78–108.

Choi, J., Edwards, J.R. & Baurle, R.A. 2009 Compressible boundary-layer predictions at high Reynolds number using hybrid LES/RANS methods. *AIAA J.* **47** (9), 2179–2193.

Chung, D. & Pullin, D.I. 2009 Large-eddy simulation and wall modelling of turbulent channel flow. *J. Fluid Mech.* **631**, 281–309.

Davidson, L. & Billson, M. 2006 Hybrid LES-RANS using synthesized turbulent fluctuations for forcing in the interface region. *Intl J. Heat Fluid Flow* **27** (6), 1028–1042.

Davidson, L. & Dahlström, S. 2005 Hybrid LES-RANS : an approach to make LES applicable at high Reynolds number. *Intl J. Comput. Fluid Dyn.* **19** (6), 415–427.

Deardorff, J.W. 1970 A numerical study of three-dimensional turbulent channel flow at large Reynolds numbers. *J. Fluid Mech.* **41** (2), 453–480.

Diosady, L.T. & Murman, S.M. 2013 Design of a variational multiscale method for high Reynolds number compressible flows. In *Proceedings of the 21st AIAA Computational Fluid Dynamics Conference*, pp. 2870.

Diosady, L.T. & Murman, S.M. 2014 DNS of flows over periodic hills using a discontinuous Galerkin spectral-element method. In *Proceedings of the 44th AIAA Fluid Dynamics Conference*, pp. 2784.

Frère, A., Carton de Wiart, C., Hillewaert, K., Chatelain, P. & Winckelmans, G. 2017 Application of wall-models to discontinuous Galerkin LES. *Phys. Fluids* **29** (8), 085111.

Gassner, G.J. & Beck, A.D. 2013 On the accuracy of high-order discretizations for underresolved turbulence simulations. *Theor. Comp. Fluid Dyn.* **27** (3-4), 221–237.

Germano, M. 1986 Differential filters of elliptic type. *Phys. Fluids* **29** (6), 1757–1758.

Germano, M., Piomelli, U., Moin, P. & Cabot, W.H. 1991 A dynamic subgrid-scale eddy viscosity model. *Phys. Fluids A: Fluid Dyn.* **3** (7), 1760–1765.

Gloerfelt, X. & Cinnella, P. 2015 Investigation of the flow dynamics in a channel constricted by periodic hills. In *Proceedings of 45th AIAA Fluid Dynamics Conference*, pp. 2480.

Gloerfelt, X. & Cinnella, P. 2019 Large eddy simulation requirements for the flow over periodic hills. *Flow Turbul. Combust.* **103** (1), 55–91.

Goc, K., Bose, S. & Moin, P. 2020 Wall-modeled large eddy simulation of an aircraft in landing configuration. In *Proceedings of AIAA Aviation 2020 Forum*, pp. 3002.

Goc, K.A., Lehmkuhl, O., Park, G.I., Bose, S.T. & Moin, P. 2021 Large eddy simulation of aircraft at affordable cost: a milestone in computational fluid dynamics. *Flow* **1**, E14.

Gravemeier, V. 2006 Scale-separating operators for variational multiscale large eddy simulation of turbulent flows. *J. Comput. Phys.* **212** (2), 400–435.

Heinz, S. 2020 A review of hybrid RANS-LES methods for turbulent flows: concepts and applications. *Prog. Aerosp. Sci.* **114**, 100597.

Hickel, S., Touber, E., Bodart, J. & Larsson, J. 2013 A parametrized non-equilibrium wall-model for large-eddy simulations. In *Eighth International Symposium on Turbulence and Shear Flow Phenomena*, Begel House Inc.

Hoyas, S., Oberlack, M., Alcántara-Ávila, F., Kraheberger, S.V. & Laux, J. 2022 Wall turbulence at high friction Reynolds numbers. *Phys. Rev. Fluids* **7** (1), 014602.

Inoue, M. & Pullin, D.I. 2011 Large-eddy simulation of the zero-pressure-gradient turbulent boundary layer up to $\mathrm{Re}\theta = \mathrm{O}(10^{12})$. *J. Fluid Mech.* **686**, 507–533.

Kawai, S. & Larsson, J. 2012 Wall-modeling in large eddy simulation: length scales, grid resolution, and accuracy. *Phys. Fluids* **24** (1), 015105.

Keating, A. & Piomelli, U. 2006 A dynamic stochastic forcing method as a wall-layer model for large-eddy simulation. *J. Turbul.* **7**, N12.

Krank, B., Kronbichler, M. & Wall, W.A. 2018 Direct numerical simulation of flow over periodic hills up to Re_H = 10,595. *Flow Turbul. Combust.* **101** (2), 521–551.

Larsson, J., Kawai, S., Bodart, J. & Bermejo-Moreno, I. 2016 Large eddy simulation with modeled wall-stress: recent progress and future directions. *Mech. Engng Rev.* **3** (1), 15–00418.

Lee, M. & Moser, R.D. 2015 Direct numerical simulation of turbulent channel flow up to. *J. Fluid Mech.* **774**, 395–415.

Lehmkuhl, O., Park, G.I., Bose, S.T. & Moin, P. 2018 Large-eddy simulation of practical aeronautical flows at stall conditions. In *Proceedings of the 2018 Summer Program*, pp. 87, Center for Turbulence Research, Stanford University.

Lv, Y., Yang, X.I.A., Park, G.I. & Ihme, M. 2021 A discontinuous Galerkin method for wall-modeled large-eddy simulations. *Comput. Fluids* **222**, 104933.

Moin, P. & Mahesh, K. 1998 Direct numerical simulation: a tool in turbulence research. *Annu. Rev. Fluid Mech.* **30** (1), 539–578.

Park, G.I. 2017 Wall-modeled large-eddy simulation of a high Reynolds number separating and reattaching flow. *AIAA J.* **55** (11), 3709–3721.

Park, G.I. & Moin, P. 2014 An improved dynamic non-equilibrium wall-model for large eddy simulation. *Phys. Fluids* **26** (1).

Park, G.I. & Moin, P. 2016*a* Numerical aspects and implementation of a two-layer zonal wall model for LES of compressible turbulent flows on unstructured meshes. *J. Comput. Phys.* **305**, 589–603.

Park, G.I. & Moin, P. 2016*b* Wall-modeled LES: recent applications to complex flows. In *Annual Research Briefs*, pp. 39–50. Center for Turbulence Research, Stanford University.

Piomelli, U. 1999 Large-eddy simulation: achievements and challenges. *Prog. Aerosp. Sci.* **35** (4), 335–362.

Piomelli, U. 2008 Wall-layer models for large-eddy simulations. *Prog. Aerosp. Sci.* **44** (6), 437–446.

Piomelli, U. & Balaras, E. 2002 Wall-layer models for large-eddy simulations. *Annu. Rev. Fluid Mech.* **34** (1), 349–374.

Piomelli, U., Balaras, E., Pasinato, H., Squires, K.D. & Spalart, P.R. 2003 The inner–outer layer interface in large-eddy simulations with wall-layer models. *Intl J. Heat Fluid Flow* **24** (4), 538–550.

Piomelli, U., Ferziger, J., Moin, P. & Kim, J. 1989 New approximate boundary conditions for large eddy simulations of wall-bounded flows. *Phys. Fluids A: Fluid Dyn.* **1** (6), 1061–1068.

Pope, S.B. 2000 *Turbulent Flows*. Cambridge University Press.

Pradhan, A. & Duraisamy, K. 2023 A unified understanding of scale-resolving simulations and near-wall modelling of turbulent flows using optimal finite-element projections. *J. Fluid Mech.* **955**, A6.

Quadrio, M., Frohnapfel, B. & Hasegawa, Y. 2016 Does the choice of the forcing term affect flow statistics in dns of turbulent channel flow? *Eur. J. Mech.-B/Fluids* **55**, 286–293.

Rapp, C. & Manhart, M. 2011 Flow over periodic hills: an experimental study. *Exp. Fluids* **51** (1), 247–269.

Reichardt, H. 1951 Vollständige darstellung der turbulenten geschwindigkeitsverteilung in glatten leitungen. *Z. Angew. Math. Mech.* **31** (7), 208–219.

Roe, P.L. 1981 Approximate Riemann solvers, parameter vectors, and difference schemes. *J. Comput. Phys.* **43** (2), 357–372.

Sagaut, P. 2005 *Large Eddy Simulation for Incompressible Flows: an Introduction*. Springer Science & Business Media.

Schumann, U. 1975 Subgrid scale model for finite difference simulations of turbulent flows in plane channels and annuli. *J. Comput. Phys.* **18** (4), 376–404.

Shur, M.L., Spalart, P.R., Strelets, M. & Travin, A.K. 2008 A hybrid RANS-LES approach with delayed-DES and wall-modelled LES capabilities. *Intl J. Heat Fluid Flow* **29** (6), 1638–1649.

Slotnick, J.P., Khodadoust, A., Alonso, J., Darmofal, D., Gropp, W., Lurie, E. & Mavriplis, D.J. 2014 CFD vision 2030 study: a path to revolutionary computational aerosciences. *NASA Contractor Rep.* 2014-218178.

Smits, A.J. & Marusic, I. 2013 Wall-bounded turbulence. *Phys. Today* **66** (9), 25–30.

Wang, M. & Moin, P. 2002 Dynamic wall modeling for large-eddy simulation of complex turbulent flows. *Phys. Fluids* **14** (7), 2043–2051.

Whitmore, M., Bose, S.T. & Moin, P. 2024 Slip-wall-modeled large-eddy simulation for prediction of turbulent smooth-body separation. In *Proceedings of AIAA SCITECH. 2024 Forum*, pp. 2374.

Whitmore, M.P. & Bose, S.T. 2023 *Evaluation of an Optimal Slip Wall Model for Large-Eddy Simulation*. Center for Turbulence Research Annual Research Briefs.

Whitmore, M.P., Griffin, K.P., Bose, S.T. & Moin, P. 2021 *Large-Eddy Simulation of a Gaussian Bump with Slip-Wall Boundary Conditions*. Center for Turbulence Research Annual Research Briefs.

Wilcox, D.C. 1998 *Turbulence Modeling for CFD*. Vol. 2. DCW industries La Canada.

Yang, X.I.A. & Bose, S.T. 2017 A physical basis of the slip-wall model for wall-modeled large-eddy simulations. In *Proceedings of 10th International Symposium on Turbulence and Shear Flow Phenomena (TSFP10)*.

Zhou, Z., He, G. & Yang, X. 2021 Wall model based on neural networks for LES of turbulent flows over periodic hills. *Phys. Rev. Fluids* **6** (5), 054610.